JGP Journal of General Physiology

ARTICLE

Spike frequency–dependent inhibition and excitation of neural activity by high-frequency ultrasound

Martin Loynaz Prieto[1], Kamyar Firouzi[2], Butrus T. Khuri-Yakub[2], Daniel V. Madison[1], and Merritt Maduke[1]

Ultrasound can modulate action potential firing in vivo and in vitro, but the mechanistic basis of this phenomenon is not well understood. To address this problem, we used patch-clamp recording to quantify the effects of focused, high-frequency (43 MHz) ultrasound on evoked action potential firing in CA1 pyramidal neurons in acute rodent hippocampal brain slices. We find that ultrasound can either inhibit or potentiate firing in a spike frequency–dependent manner: at low (near-threshold) input currents and low firing frequencies, ultrasound inhibits firing, while at higher input currents and higher firing frequencies, ultrasound potentiates firing. The net result of these two competing effects is that ultrasound increases the threshold current for action potential firing, the slope of frequency-input curves, and the maximum firing frequency. In addition, ultrasound slightly hyperpolarizes the resting membrane potential, decreases action potential width, and increases the depth of the after-hyperpolarization. All of these results can be explained by the hypothesis that ultrasound activates a sustained potassium conductance. According to this hypothesis, increased outward potassium currents hyperpolarize the resting membrane potential and inhibit firing at near-threshold input currents but potentiate firing in response to higher-input currents by limiting inactivation of voltage-dependent sodium channels during the action potential. This latter effect is a consequence of faster action potential repolarization, which limits inactivation of voltage-dependent sodium channels, and deeper (more negative) after-hyperpolarization, which increases the rate of recovery from inactivation. Based on these results, we propose that ultrasound activates thermosensitive and mechanosensitive two-pore-domain potassium (K2P) channels through heating or mechanical effects of acoustic radiation force. Finite-element modeling of the effects of ultrasound on brain tissue suggests that the effects of ultrasound on firing frequency are caused by a small (<2°C) increase in temperature, with possible additional contributions from mechanical effects.

Introduction

Ultrasound can noninvasively modulate action potential activity in neurons in vivo and in vitro, with improved depth penetration and spatial resolution relative to other noninvasive neuromodulation modalities, and it may therefore become an important new technology in basic and clinical neuroscience (Fry et al., 1958; Gavrilov et al., 1996; Tufail et al., 2010; Bystritsky et al., 2011; Fomenko et al., 2018; Blackmore et al., 2019). Investigation of this phenomenon has predominantly focused on low-frequency ultrasound (defined here as <3 MHz, although there is no firmly defined boundary between "high" and "low" frequency in the neuromodulation field), but higher ultrasound frequencies have also been shown to modulate action potential firing in vitro (Menz et al., 2013, 2019) and to directly modulate ion channel activity in heterologous systems (Kubanek et al., 2016; Prieto et al., 2018). The focus on lower-frequency ultrasound is understandable, since envisioned clinical applications involving transcranial focused ultrasound have been a primary motivation for research on ultrasound neuromodulation, and loss of ultrasound power due to attenuation in the skull limits these applications to low-frequency ultrasound. For applications in which transmission through the skull does not impose limits on frequency, such as in vitro studies, neuromodulation in the peripheral nervous system (Downs et al., 2018; Cotero et al., 2019; Zachs et al., 2019), neuromodulation using subcranial implants, or neuromodulation in experimental animal model systems involving craniotomies or acoustically transparent cranial windows, high frequencies have a distinct advantage in terms of the greater spatial resolution that can be achieved. Even for in vivo applications in human subjects, however, the spatial resolutions that can be achieved with low-frequency, transcranial ultrasound neuromodulation are on the order of millimeters, making ultrasound neuromodulation superior in this respect to other, more established forms of noninvasive brain stimulation (Tyler et al., 2018).

[1]Department of Molecular and Cellular Physiology, Stanford University, Stanford, CA; [2]E.L. Ginzton Laboratory, Stanford University, Stanford, CA.

Correspondence to Merritt Maduke: maduke@stanford.edu; Martin Loynaz Prieto: prieto@stanford.edu.

These applications motivate investigation of the fundamental physical, cellular, and molecular mechanisms underlying neuromodulation, which are all not well understood for either high- or low-frequency ultrasound. It remains an open question to what extent these mechanisms overlap for high- and low-frequency ultrasound neuromodulation. In terms of the basic physical mechanism by which acoustic energy is transduced into effects on biological tissue, most proposed mechanisms for ultrasound neuromodulation involve heating due to absorption of acoustic energy (Hand, 1998), mechanical effects of acoustic radiation force (Duck, 1998; Sarvazyan et al., 2010), or effects of cavitation (the nucleation, growth, oscillation, and sometimes collapse of microscopic gas bubbles; Leighton, 1998; Wu and Nyborg, 2008; Krasovitski et al., 2011; Plaksin et al., 2016). Of these, the first two increase with acoustic frequency, while the probability of cavitation decreases with acoustic frequency. There are also many unanswered questions at the cellular level. Both excitatory and inhibitory effects of ultrasound have been observed using direct or indirect measures of neural activity at the population level (Bystritsky et al., 2011; Blackmore et al., 2019), but it is unclear whether the direct effect of ultrasound at the cellular level is excitatory or inhibitory. Of course, the answer to this question could depend on any number of possible relevant biological and experimental variables, such as species, tissue, specific neural subtype, ultrasound stimulus parameters, or whether effects on intrinsic or evoked activity are measured. For example, a cellular-level excitatory effect, specific to inhibitory interneurons, could produce an inhibitory effect at the population level. This leads to the question of whether certain subpopulations of neurons are more sensitive to ultrasound than others, and if so, what specific molecular mechanisms underlie the differences in sensitivity. Do certain ion channels respond directly to ultrasound? What biophysical properties might account for the sensitivity of these channels to ultrasound, and how might cell type–specific differences in the density and localization of these channels, and the way in which they interact with other ion channels to regulate action potential firing, produce differences in the response to ultrasound?

One reason there are so many outstanding questions regarding ultrasound neuromodulation is that patch-clamp recordings of the effects of ultrasound on action potential firing in neurons have been unavailable. At low ultrasound frequencies, we (Prieto et al., 2018) and others (Tyler et al., 2008) have found that patch-clamp seals are extremely unstable in the presence of ultrasound, precluding detailed, mechanistic studies of ultrasound neuromodulation with this technique, which provides quantitative information on action potential timing and dynamics unobtainable with other techniques. However, we have previously shown that stable patch-clamp recordings can be achieved using ultrasound at the frequency of 43 MHz (Prieto et al., 2018). Here, we use patch-clamp recording to measure the effects of ultrasound at 43 MHz and 50 W/cm^2 on action potential firing in response to injected current in pyramidal neurons of the CA1 layer of the hippocampus in acute rodent brain slices. We find that ultrasound has a bidirectional, spike frequency–dependent effect on excitability, and that this and other observed neurophysiological effects of ultrasound can be explained by activation by ultrasound of a steady K^+ current, resembling that of two-pore-domain potassium (K2P) channels.

Materials and methods

Slice preparation

Brain slices were prepared from male Sprague–Dawley rats, 35–50 d old. Rats were anesthetized with isofluorane and decapitated, and the brain was immediately removed and placed in ice-cold artificial cerebral spinal fluid (ACSF), bubbled with 95% O_2 and 5% CO_2. The hippocampus was dissected out and placed on the slicing apparatus, consisting of a manual micrometer and a gravity-driven vertical slicing mechanism, with the CA1 layer oriented approximately parallel to the slicing blade. Slices (500 microns thick) were prepared and then stored in a humidified chamber with an atmosphere of 95% O_2/5% CO_2, resting on a square of filter paper placed on a dish of ACSF. Slices were used within 1–6 h of slice preparation. Animals were handled in accordance with protocols approved by Stanford University's Institutional Animal Care and Use Committee.

Ultrasound

Continuous-wave ultrasound at 43 MHz and 50 W/cm^2 was applied to brain slices using a setup similar to that we previously used for our experiments on cultured cells (Prieto et al., 2018), except that the tissue was visualized with a dissecting microscope at low magnification. The bottom of the experimental chamber was a 25-micron film of polystyrene, plasma-treated with a Harrick plasma cleaner (Harrick Plasma). Ultrasound was transmitted from below (through the polystyrene film) with the sound beam perpendicular to the bottom of the chamber. The 43-MHz transducer was a custom-built device, calibrated as described previously (Prieto et al., 2013), excited using an ENI 403LA (37 dB) amplifier (ENI). The focal volume of the transducer is approximately a cylinder 90 microns in diameter by 500 microns long, and the focal distance is ∼4.2 mm. The setup was based on the stage from a Zeiss Axioskop-2 microscope (Zeiss Microscopes), with the housing for the sub-stage condenser modified to accommodate the transducer, such that the position of the transducer could be adjusted using the controls for alignment of the condenser, and the position of the tissue sample relative to the transducer could be adjusted with the microscope stage. The transducer was coupled to the polystyrene film at the bottom of the experimental chamber using a small volume of distilled water held in place by a rubber O-ring attached to the tip of the transducer with silicone grease. The focal volume of the transducer was aligned along the z axis using a pulse-echo protocol, adjusting the height of the transducer to maximize the echo signal from the bottom of the empty chamber. The focus was aligned in the x-y plane by adding to the chamber a small volume of ACSF, barely sufficient to cover the bottom of the chamber, such that a thin layer of solution was spread over the bottom of the chamber. Ultrasound pulses, 1 s in length, were then applied, raising a mound of fluid at the focus of the transducer (due to the radiation force produced by reflection of the acoustic wave at the interface between the solution and the air above it; Duck, 1998). The mound of fluid was

then aligned in the x-y plane to the center of a reticle in one eyepiece of the dissecting microscope, and, after adding additional ACSF and the tissue sample to the chamber, the center of the reticle was aligned with the region of the tissue targeted for patch-clamp recording. The ultrasound intensity (50 W/cm^2) is the spatial peak, pulse average intensity for the free field. The interval between ultrasound applications was at least 12 s.

Electrophysiology

Current clamp recordings were performed using an Axon Instruments Axoclamp-2B amplifier operating in "Bridge" mode and a Digidata 1330A digitizer with pClamp software (Molecular Devices), except for the preliminary experiments in Fig. S1, which were performed with an Axon Instruments Axopatch 200B amplifier (Molecular Devices). Patch-clamp recording was performed using a "blind-patch" approach (Blanton et al., 1989; Malinow and Tsien, 1990; Castañeda-Castellanos et al., 2006), in which the recording pipette was positioned above the CA1 layer of the hippocampus, as identified visually at low magnification, and then slowly lowered into the tissue while applying positive pressure to the pipette and monitoring the pipette tip resistance in voltage-clamp mode. In the blind-patch approach, a small decrease in tip resistance is used to indicate possible contact of the pipette tip with a neuron in the absence of the usual visual cues. Typically, the first two instances of possible cell contact were not used, to avoid patching on cells at the surface of the tissue that may have been damaged during the slicing procedure. Gigaseals and the subsequent whole-cell recording configuration were obtained following the standard procedure in voltage-clamp mode before switching to current-clamp mode. In most experiments, slices were held in place with a Warner Instruments RC-22 slice anchor (Harvard Bioscience); the experiments in Fig. S1 and some of the experiments in Fig. 1 E were performed without a slice anchor. No obvious effects of the slice anchor on the ultrasound response were noted. Series resistance, monitored and compensated throughout the recording, was between 30 and 100 MΩ. All of the neurons used for experiments could be unambiguously identified as pyramidal cells by their distinct adaptive firing patterns in response to 2-s current steps. Current records were low-pass filtered at 10 kHz and sampled at 100 kHz. Brain slices were continuously perfused with ACSF (in mM: 119 NaCl, 2.5 KCl, 1.3 $MgSO_4$, 2.5 $CaCl_2$, 1 NaH_2PO_4, 26.2 $NaHCO_3$, and 11 glucose), bubbled with 95% O_2/5% CO_2, at ∼100–250 ml/h. The internal solution was (in mM) 126 K-gluconate, 4 KCl, 10 HEPES, 4 Mg-ATP, 0.3 Na_2-guanosine triphosphate, 10 Na-phosphocreatine, 10 sucrose, and 50 U/ml creatine phosphokinase (porcine), pH 7.2 (KOH). This internal solution contains an ATP-regenerating system (phosphocreatine and creatine phosphokinase) because we found that the strength of the response to ultrasound was unstable, gradually declining over the course of a recording unless the ATP-regenerating system was included (Fig. S2). Na-phosphocreatine was obtained from Abcam, and creatine phosphokinase was obtained from EMD Millipore. All other salts and chemicals were obtained from either Sigma-Aldrich or Thermo Fisher Scientific (For some of the preliminary recordings shown in Fig. 1 E, the creatine phosphokinase was omitted from the internal solution, or a different internal solution, containing [in mM] 120 K-gluconate, 40 HEPES, 5 $MgCl_2$, 0.3 Na_2-guanosine triphosphate, and 2 Na_2ATP, pH 7.2 [KOH], was used. Creatine phosphokinase was also omitted for the experiments in Fig. S4. Other than the reduction of the ultrasound response over time in the absence of creatine phosphokinase, no obvious differences in recordings with different internal solutions were noted). Because creatine phosphokinase increases the viscosity of the solution, making it difficult to obtain gigaseals, a small volume of internal solution without the enzyme was added to the tip of the pipette (enough to fill approximately the first 3 mm of the tip) before back-filling the pipette with the enzyme-containing solution. Pipettes were pulled from thick-walled glass and had resistances between 5 and 10 MΩ. Recordings were performed at room temperature (21–23°C), except for the experiments in Fig. S4, which were performed at near physiological temperature (30°C). For these experiments, the temperature of the external solution was regulated and monitored with a Warner Instruments CL-100 bipolar temperature controller equipped with a SC-20 in-line heater/cooler and a thermistor (Warner Instruments). The external solution was heated to 35–37°C while being bubbled with 95% O_2/5% CO_2 and then passed through the heater/cooler and cooled to achieve the target temperature of 30°C in the bath solution (The external solution was cooled rather than heated to avoid loss of oxygen tension and formation of gas bubbles due to heating of oxygen-saturated solution).

Data analysis

Current records were analyzed in Igor Pro (Wavemetrics) with user-written procedures. Action potential threshold was defined as the point at which the first derivative of the voltage reached 4% of its peak value during the rising phase of the action potential. This quantitative criterion was previously found to correspond with action potential thresholds as identified visually (Khaliq and Bean, 2010; Yamada-Hanff and Bean, 2015), and we found that it also works well with our data, using phase plots to visually confirm the threshold value. Action potential height was defined as the difference between the action potential peak and the action potential threshold voltage. Action potential width was measured at 50% of action potential height defined in this manner. Threshold current levels for action potential firing were estimated based on a series of current steps in 10-pA increments. Frequency-input (f-i) plots and action potential parameters (height, width, latency, and interspike intervals) were determined from the average values of at least three trials each for the control and ultrasound conditions. F-i trials were performed alternatingly for the control and ultrasound conditions, with the first condition tested varying randomly on a cell-by-cell basis.

Average traces for analysis of the effects of ultrasound on membrane resting potential and membrane capacitance were derived from at least three voltage traces. Statistical significance was assessed using paired or unpaired two-tailed Student's *t* tests, with $P < 0.05$ defined as significant. Statistical analysis was performed in Microsoft Excel.

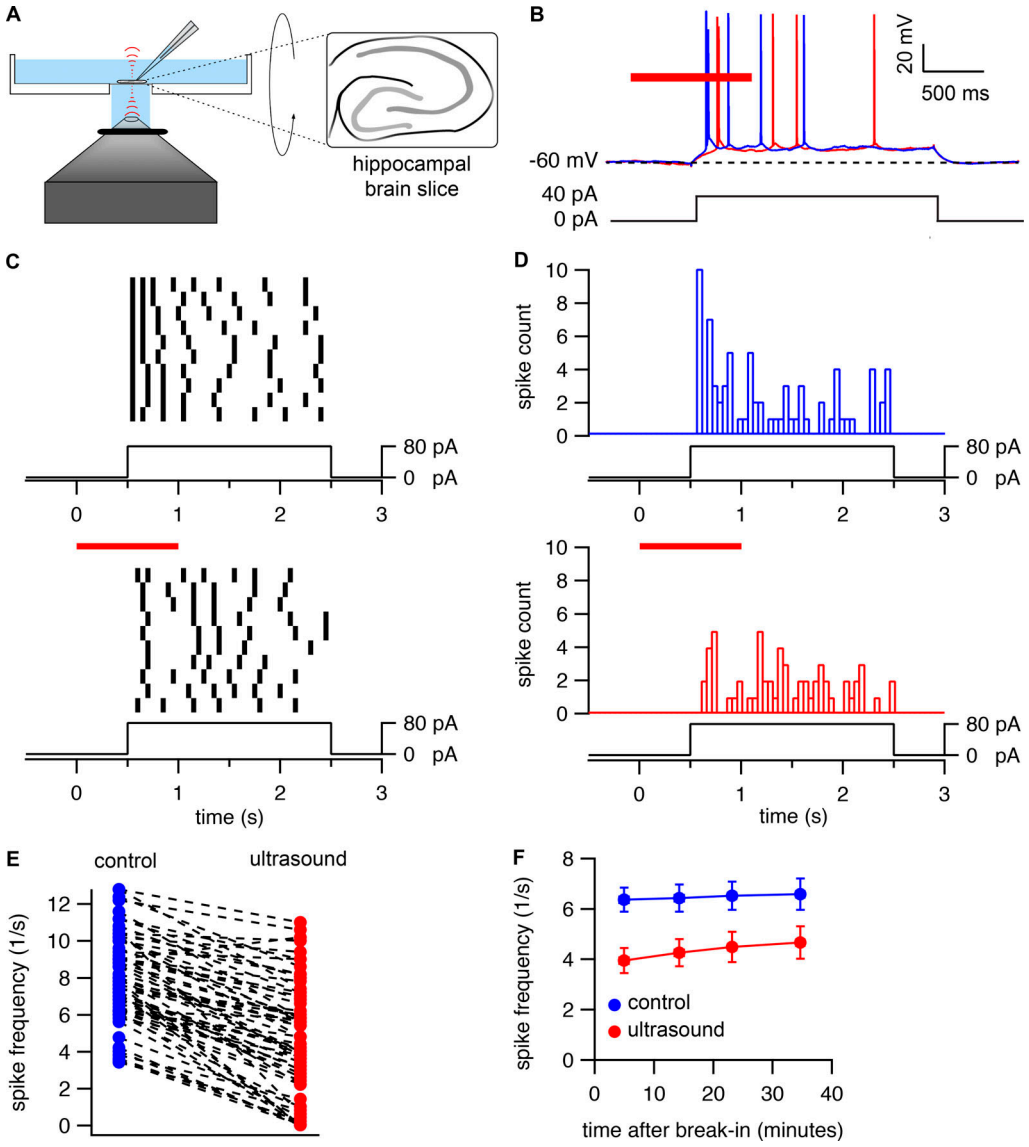

Figure 1. **Consistent inhibition of action potential firing by high-frequency ultrasound. (A)** Diagram of experimental setup. Ultrasound is applied to 500-micron hippocampal brain slices resting on a 25-micron film of polystyrene. The 43-MHz focused transducer is located below the experimental chamber, with ultrasound propagating perpendicular to the bottom of the recording chamber. **(B)** Experimental protocol and example voltage traces showing inhibition of action potential firing by ultrasound. A 1-s, continuous-wave ultrasound pulse at 43 MHz and 50 W/cm^2 (red bar) is applied 500 ms before the start of a 2-s current injection. Voltage traces are shown in the presence (red) and absence (blue) of the ultrasound stimulus. The dashed line indicates the resting membrane voltage. **(C)** Example raster plots showing a consistent effect of ultrasound on firing frequency. The results of 20 consecutive trials of the protocol in B, alternating between the control (top) and ultrasound (bottom) conditions, are shown. The voltage traces were divided into 50-ms bins; a solid black bin indicates that an action potential occurred within that particular time bin. Time is relative to the start of the ultrasound pulse. **(D)** Spike-time histograms prepared by summing the 10 trials for the control (top, blue bars) and ultrasound (bottom, red bars) conditions from C. **(E)** Summary of the effects of ultrasound for n = 66 cells. The average firing frequency during the first 500 ms of the current step is shown for the control (blue) and ultrasound (red) conditions. **(F)** Stability of the ultrasound response. Mean (± SEM, n = 10 cells) spike frequencies during the first 500 ms of a current step in the presence (red circles) and absence (blue circles) of ultrasound for the protocol shown in B, as a function of time relative to break-in (establishment of whole-cell recording configuration). Spike frequencies were measured at various time points between 0 and 10, 10 and 20, 20 and 30, and 30 and 40 min after break-in. The x values represent the mean start time for the protocol to measure spike frequencies (which comprised 2 min of recording time). The amplitude of the current step was adjusted over time to maintain spiking behavior as close as possible to that at the start of the experiment.

Finite-element simulations

Finite-element simulations were performed in COMSOL (COMSOL Inc.). The simulation domain had radially symmetric geometry and was 6 mm in the axial direction. The simulation domain contained four layers of different materials: a lower layer of water (4.2 mm thick in the axial direction), followed by a layer of polystyrene (25 microns thick), followed by a layer of brain tissue (500 microns thick), followed by an upper layer of water (1.275 mm thick). The width of the simulation domain in the axial direction was 1 mm (for simulation of acoustic pressure and heating) or 5 mm (for simulation of mechanical deformation) in the axial direction. A 940-micron-diameter by

Table 1. **Values of material properties used in finite-element simulations**

	Water	Polystyrene	Brain tissue
Density (kg/m^3)	1,000[a]	1,040[b]	1,007[c]
Speed of sound (m/s)	1,500[a]	2,300[b]	1,538[c]
Attenuation coefficient at 43 MHz (neper/m)	46[d]	160[e]	253[f]
Heat capacity (J/kg·K)	4,180[a]	1,200[g]	3,500[h]
Thermal conductivity (W/m·K)	0.6[a]	0.1[g]	0.5[h]
Young's modulus (Pa)	Not applicable	10^9[i]	500[j]
Poisson's ratio	Not applicable	0.4[i]	0.4998[k]
Shear viscosity (Pa·s)	Not applicable	Not applicable	1[l]

[a]Standard value.
[b]Based on typical acoustic properties of plastics (Selfridge, 1985).
[c]Following Menz et al. (2019), based on Thijssen et al. (1985).
[d]Chemical Rubber Company, 1965.
[e]Measured (Prieto et al., 2018)
[f]Following Menz et al. (2019), based on de Korte et al. (1994).
[g]Based on typical thermal properties of plastics (Gaur and Wunderlich, 1982; Harper, 2006).
[h]Typical values for soft tissues (Hand, 1998).
[i]Based on typical mechanical properties of plastics (Harper, 2006).
[j]Menz et al. (2019), from measurements of ultrasound-induced displacement in the retina.
[k]Tissue assumed to be incompressible for small deformations.
[l]See text under Physical mechanism of neuromodulation by high-frequency ultrasound.

100-micron-height arc on the lower axial boundary of the simulation domain represented the quartz lens of the transducer.

Simulations of acoustic pressure, heating, and static displacement in response to radiation force were performed as described previously (Prieto et al., 2018). For simulation of dynamic tissue displacement in response to radiation force, the brain slice was modeled as a incompressible, linear viscoelastic material (Calhoun et al., 2019), characterized by Young's modulus, Poisson's ratio, and shear viscosity, loaded by the fluid layer above it. The polystyrene was modeled as a linear elastic material, because we determined in a series of simulations that including viscosity of the polystyrene had no effect on the tissue displacement. A time step of 0.1 ms was used for simulation of the dynamic tissue displacement. Material properties used for water, polystyrene, and brain tissue used in the simulation and sources for these values are given in Table 1. Additional details on mesh size, boundary conditions, and solver configurations are available in Prieto et al. (2018).

Online supplemental material

Fig. S1 shows the effect of ultrasound at different intensities on action potential firing frequency. Fig. S2 displays stabilization of the response to ultrasound by an ATP-regenerating system in the internal solution. Fig. S3 depicts the effect of ultrasound on action potential height. Fig. S4 shows the effects of ultrasound on action potential firing and waveform at near physiological temperature (30°C).

Results

We measured the effects of ultrasound on action potential firing in hippocampal CA1 pyramidal cells using the setup shown in Fig. 1 A (described in Materials and methods). Throughout the experiments reported here, ultrasound was applied at 43 MHz and 50 W/cm^2 as a 1-s, continuous-wave pulse. In an initial exploration of the effects of intensity on the ultrasound response, we determined that 50 W/cm^2 had a sufficiently robust effect on firing frequency to permit quantitative investigation of this effect (Fig. S1), but we did not perform a detailed investigation of the intensity dependence. We chose to use continuous-wave ultrasound (without additional low-frequency modulation within the pulse) because continuous-wave ultrasound was previously found to be optimal for ultrasound neuromodulation of retinal ganglion cells at 43 MHz (Menz et al., 2013). With these ultrasound parameters, we found robust, reproducible inhibition of action potential firing by ultrasound using the protocol illustrated in Fig. 1 B. In these experiments, a current-injection amplitude sufficient to induce firing at an average frequency of ∼4–12 Hz during the first 500 ms of the current step (corresponding to the overlap between the ultrasound stimulus and current step) was used. This range of firing frequencies is physiologically relevant and sufficient to detect either inhibition or potentiation of firing. With these experimental conditions, we established that the response to ultrasound is highly reproducible, both on a trial-by-trial basis within the same cell (Fig. 1, C and D) and between cells, with similar effects seen in >50 cells (Fig. 1 E). In addition, the response to ultrasound was stable over the course of recordings lasting over 30 min (Fig. 1 F and Fig. S2); in a few cases where the patch seal lasted for >90 min, the ultrasound response remained stable.

Effects of ultrasound on f-i curves

To explore the effects of ultrasound on excitability over a wider range of firing frequencies, we generated f-i curves comparing average firing frequencies as a function of input current in the presence and absence of ultrasound. An example f-i curve generated with the protocol illustrated in Fig. 1 B is shown in Fig. 2 A, along with example voltage traces in Fig. 2 B. The average spike frequency during the first 500 ms of the current step was compared with the spike frequency in the same time window in the absence of ultrasound. To compare the effects of ultrasound across neurons, we converted the f-i curves into plots of the relative increase or decrease in firing frequency as a function of the input current (Fig. 2, C and D). These data reveal two distinct regimes with contrasting inhibitory and excitatory ultrasound effects. At relatively low input currents, near the threshold for action potential firing under this current stimulation protocol, ultrasound decreases the average firing frequency, while at relatively high input currents, well above the action potential threshold, ultrasound increases the average firing frequency. Between these two regimes, there is a transitional region where

there is little or no effect on average firing frequency, presumably due to the balance between competing inhibitory and excitatory effects. Other notable effects of ultrasound on the f-i curves are an increase in the threshold current for action potential firing, an increase in the slope of the f-i relationship in the approximately linear region of the f-i curve, and an increase in the maximum firing frequency in the sublinear "plateau" region of the curve (Fig. 2 A). The mean (± SEM) slope of linear region of the f-i curve increased from 0.108 ± 0.007 Hz/pA in the control condition to 0.145 ± 0.012 Hz/pA in the ultrasound condition; the mean maximum firing frequency increased from 23 ± 1 Hz in the control condition to 30 ± 2 Hz in the ultrasound condition (n = 9).

Action potential firing behavior is determined by the interaction between numerous K^+, Na^+, and other ionic currents (Madison and Nicoll, 1984; Bean, 2007). Some of these currents are clearly identified with specific ion channel subtypes, while the molecular identity of others is still uncertain. Thus, f-i curves are a complicated function of the density, localization, conductance, and kinetic properties of these channels/currents. Some currents inactivate relatively rapidly and only influence firing frequency during the initial response to a sustained depolarizing current step, while others show slow, voltage-dependent activation, and only influence firing frequency late in a current step. Still other currents can influence firing frequency throughout a sustained depolarization. To explore the molecular basis of the response to ultrasound, we therefore generated a second set of f-i curves with ultrasound applied 1 s after the start of a 3-s current step (Fig. 3 A).

Ultrasound also had a bidirectional, spike frequency–dependent effect on excitability when it was applied 1 s after the start of a current step (Fig. 3). Again, ultrasound decreased firing frequency in the low-firing frequency, near-threshold region of the f-i curve, and increased spike rate in the high-firing frequency, suprathreshold region of the curve (Fig. 3, B–D). However, the excitatory effect was more pronounced than we observed when the ultrasound pulse started 500 ms before the start of the current step. Here, ultrasound potentiated firing frequency by several hundred percent for high input currents (Fig. 3 D), as compared with a maximum potentiation of 49 ± 16% at 450 pA seen with the earlier ultrasound application (Fig. 2 C). This reflects the fact that in response to prolonged injection of high-amplitude currents, accumulation of voltage-gated Na^+ (Na_V) channel inactivation can drive pyramidal cells into a refractory state where spiking is infrequent and irregular or entirely absent (for example, the voltage trace for the control condition at +450 pA in Fig. 3 C shows an initial steep decline in action potential height, followed by a gradual partial recovery of action potential height, followed by a period of no action potential activity). If neurons are in this refractory state during the ultrasound application, ultrasound can "rescue" firing (as in the example voltage trace for the ultrasound condition at +450 pA in Fig. 3 C). This refractory state probably does not occur under normal physiological conditions, but the ability of ultrasound to rescue action potential firing under these conditions still provides an important clue as to the molecular mechanisms underlying the effects of ultrasound on firing frequency, as

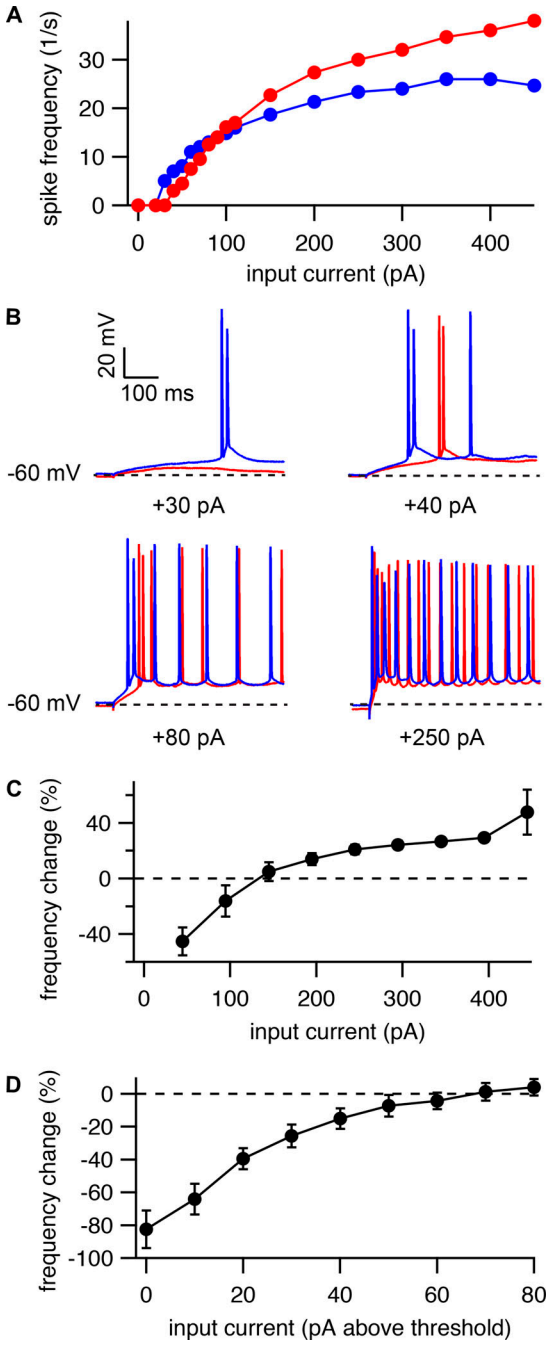

Figure 2. **Ultrasound can inhibit or potentiate action potential firing. (A)** Example f-i curve showing average firing frequency during the first 500 ms of a current step as a function of input current, with (red) and without (blue) a 1-s ultrasound pulse starting 500 ms before the start of the current step. Each point represents the average of three trials on the same cell. **(B)** Example voltage traces for the cell in A showing action potential firing during the first 500 ms of current steps to +30, +40, +80, or +250 pA, with (red) and without (blue) ultrasound. The dashed lines indicate the approximate resting membrane voltage of −60 mV. **(C)** Mean (± SEM, n = 9 cells) change in spike frequency in response to ultrasound as a function of input current. **(D)** Inhibition is strongest near threshold. Mean (± SEM, n = 7 cells) change in spike frequency in response to ultrasound as a function of input current relative to the threshold current for action potential firing, for near-threshold currents.

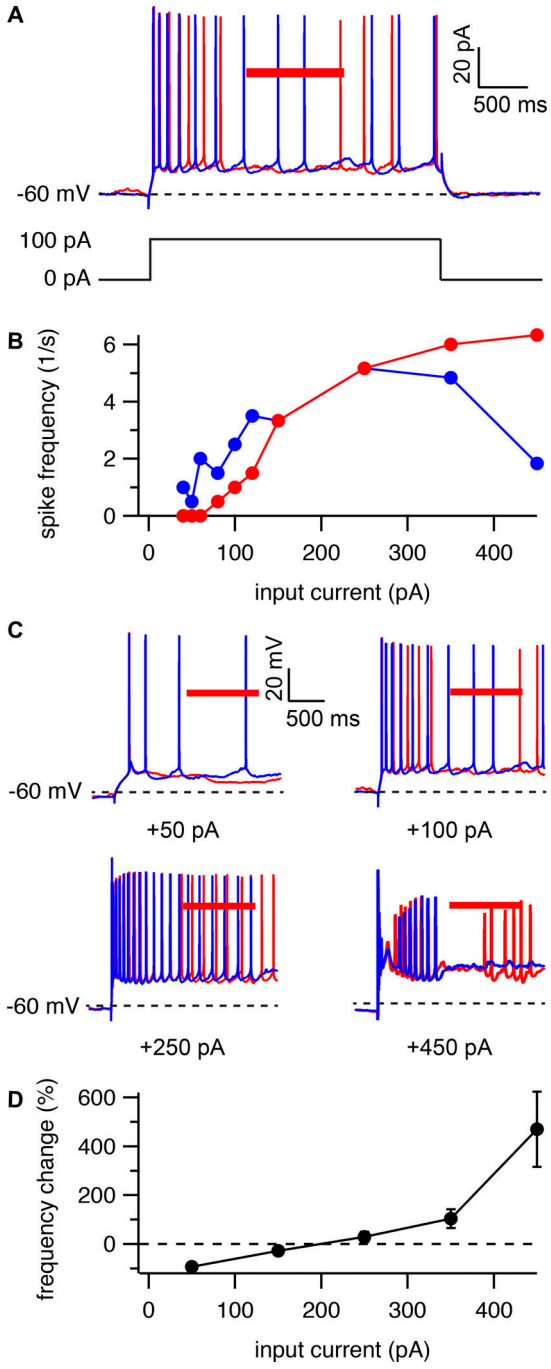

Figure 3. **Ultrasound can also inhibit or potentiate action potential firing when applied late in a current step. (A)** Experimental protocol and example voltage traces with (red) and without (blue) ultrasound. Ultrasound is applied 1 s after the start of a 3-s current step. The dashed line indicates the resting membrane voltage. **(B)** Example f-i curve showing average firing frequency during the ultrasound application for the protocol in A (red) and during the same time window without ultrasound (blue), as a function of input current. Each point represents the average of three trials on one cell. **(C)** Example voltage traces for the cell in B showing action potential firing during the ultrasound application (red) and during the same time window without ultrasound (blue) in response to current steps to +50, +100, +250, or +450 pA. The dashed lines indicate the approximate resting membrane voltage of −60 mV. **(D)** Mean (± SEM) change in spike frequency in response to ultrasound as a function of input current (n = 3 cells at +50 pA; n = 6 cells at all other input currents; in three cells, the firing frequency at +50 pA was zero for both the control and ultrasound conditions).

discussed further below. A hint of this rescue phenomenon is also seen when the ultrasound application starts before the current step, as seen in the abrupt increase in the potentiation effect at +450 pA (Fig. 2 C).

Effects of ultrasound on interspike intervals

To examine the effects of ultrasound on action potential firing in more detail, we compared the latency to the first spike, and the intervals between subsequent spikes (interspike intervals), in the control and ultrasound conditions (Fig. 4). To summarize these results, and to account for the variability in intrinsic excitability between cells, we averaged instantaneous firing frequencies (latency and interspike intervals) across cells firing at approximately the same average firing frequency (5, 10, or 20 Hz) in the control condition at whatever input current was necessary to achieve these average firing frequencies, and at the same input current in the ultrasound condition (Fig. 4, A–C). We note, however, that this averaging procedure can obscure some of the details of ultrasound's effects. At 5 Hz, the effect of ultrasound applied 500 ms before the start of the current step is predominantly inhibitory (as seen in the longer average latency and interspike intervals in the ultrasound as compared with the control condition (Fig. 4 A), but the interval between the first and second spikes was actually shorter in the ultrasound condition than the control condition in some cells (6 out of 13 cells in this dataset). This effect occurs because, even at relatively low average firing frequencies, pyramidal cells will occasionally fire "doublets" or high-frequency bursts of two action potentials, in which a second action potential is triggered by the afterdepolarization of the initial action potential. When this occurs, ultrasound decreases the interval between spikes (Fig. 4 D). This result indicates that the mechanism by which ultrasound potentiates firing at high average firing frequencies is also active under conditions of low overall average firing frequency, during localized periods of high-frequency firing. A similar combination of inhibitory and excitatory effects can be observed at 10 Hz and even 20 Hz (Fig. 4, B and C). At 20 Hz, ultrasound still increased the latency to the first spike (16 ± 2 ms versus 12 ± 1 ms in the control condition; n = 12, P = 5.2 × 10^{-4}, using paired, two-tailed Student's t test), despite decreasing the interspike interval for all subsequent spikes (Fig. 4 C). The effect of ultrasound was also mixed when ultrasound was applied 1 s after the start of the current step (Fig. 4 E).

Effects of ultrasound on resting membrane potential

Ultrasound also has effects on resting membrane potential, which can be observed by averaging several voltage traces aligned to the onset of the ultrasound pulse, in the absence of injected current. As shown in Fig. 5 A, ultrasound has a slight hyperpolarizing effect on resting membrane potential. The average voltage traces also show another interesting effect of ultrasound. In addition to the relatively constant hyperpolarization, there is a transient depolarization of the resting membrane potential, preceding the hyperpolarization effect and acting on a faster time scale, at the onset of the ultrasound pulse; this transient depolarization is matched by a roughly symmetrical transient hyperpolarization at the offset

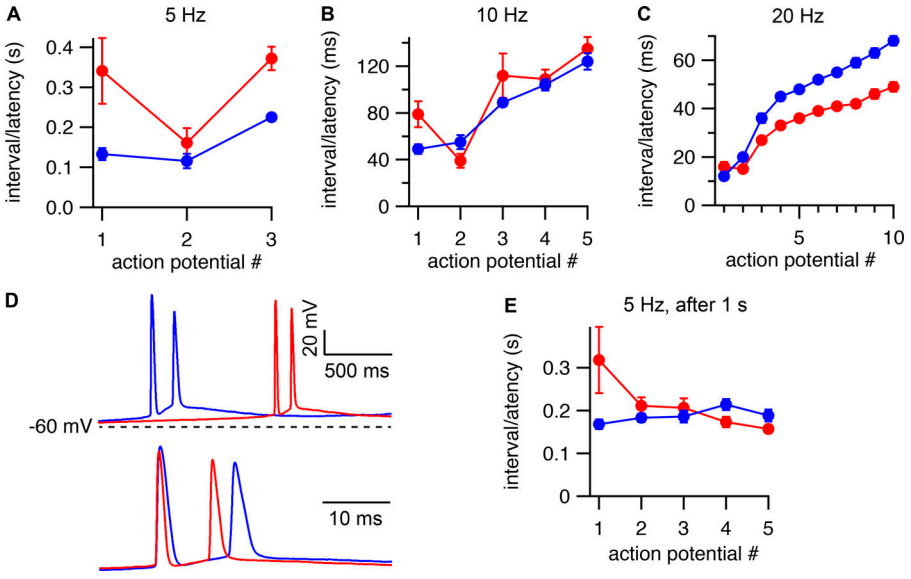

Figure 4. **Effects of ultrasound on action potential timing. (A–C)** Mean (± SEM) latency between the start of the current step and the first action potential, and mean intervals between the first and second, and second and third, etc., action potentials, for cells firing at average frequencies of ∼5 Hz (n = 13 cells), 10 Hz (n = 15 cells), and 20 Hz (n = 13 cells) during the first 500 ms of the current step, with (red) or without (blue) a 1-s ultrasound pulse starting 500 ms before the current step. The actual spike frequencies were 5.6 ± 0.1, 10.5 ± 0.2, and 20.4 ± 0.3 Hz, and the injected currents were 70 ± 7, 115 ± 9, and 292 ± 28 pA for the 5-, 10-, and 20-Hz conditions. **(D)** Example voltage traces showing decreased interval between the first and second action potentials at low average firing frequency. The top panel shows the first two action potentials for the control (blue) and ultrasound (red) conditions. The dashed line indicates the approximate resting membrane voltage of −60 mV. The bottom panel shows the same data, aligned to the action potential threshold on a zoomed-in time scale. **(E)** Same as A–C, for an average firing frequency of 5 Hz, except that ultrasound was applied 1 s after the start of a 3-s current step, and the average firing frequency and intervals/latency were determined during the ultrasound stimulus or during the same time period without ultrasound (n = 6 cells). The actual spike frequency was 5.2 ± 0.2 Hz, and the injected currents was 183 ± 21 pA.

of the pulse (Fig. 5 A, arrows). The symmetrical, on/off nature of these transients suggests that they are caused by changes in membrane capacitance, as does the fact that they occur much faster than the steady-state changes in resting membrane potential (Fig. 5, A–C; changes in membrane potential due to changes in capacitance can occur much faster than those due to ionic currents because they do not involve actual redistribution of charges across the membrane and are therefore not limited by membrane conductance). Thus, the results in Fig. 5 can be described by three distinct steps: (1) ultrasound rapidly increases membrane capacitance (C) at the onset of the ultrasound pulse, which causes the membrane voltage (V) to become less negative (due to an increase in the denominator in the equation V = Q/C, where Q is the negative total charge on the membrane); (2) ionic currents then slowly change the membrane voltage to a steady-state value determined by the total ionic current (one or more ion channels having been affected by ultrasound) resulting in membrane hyperpolarization; (3) at the offset of the ultrasound pulse, capacitance rapidly relaxes back to its initial value, producing a transient decrease in membrane voltage, through essentially the same mechanism as in step 1. We investigate the physical basis of these capacitance changes and their relationship to the effects of ultrasound on excitability below, but one point worth mentioning here is that the change in capacitance is too small for its effect on the rate of membrane charging (less than 1% change in membrane time constant) to have a significant effect on excitability in and of itself.

The K2P channel hypothesis

What ion channels might be responsible for the effects of ultrasound on excitability and resting membrane potential? A compelling hypothesis—able to explain all of our data—is that ultrasound activates a fast-activating, noninactivating potassium channel, such as members of the K2P potassium channel family which includes TWIK (tandem of p domains in a weak inward rectifying K^+ channel), TREK (TWIK-related K^+ channel), TASK (TWIK-related acid-sensitive K^+ channel), and TRAAK (TWIK-related arachadonic acid–stimulted K^+ channel) channels. While commonly described as "voltage-independent," K2P channels (with the exception of TWIK-1 channels) actually have

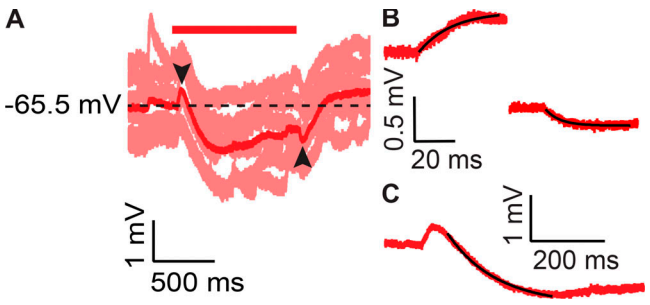

Figure 5. **Effects of ultrasound on resting membrane potential and membrane capacitance. (A)** Six individual voltage traces (pink) and the average of these voltage traces (red) showing the effect of ultrasound (red bar) on resting membrane potential. The black arrows indicate transients due to changes in membrane capacitance. The dashed line indicates the mean resting membrane voltage. **(B)** Zoomed-in timescale showing the fast voltage transients (black arrows in A) for ultrasound onset (top left) and offset (bottom right). Exponential fits (black lines) to the rise and fall of the voltage transients give amplitudes and time constants of 0.45 mV and 16.3 ms for the onset and 0.22 mV and 6.7 ms for the offset, for the example shown; mean values (± SEM) were 0.41 ± 0.04 mV and 10.4 ± 1.2 ms for the onset and 0.35 ± 0.04 mV and 9.7 ± 1.7 ms for the offset (n = 15). No significant differences were found between the time constants (P = 0.73) or the amplitude (P = 0.087) of the transients (paired, two-tailed Student's t tests). **(C)** Slow membrane hyperpolarization in response to ultrasound from the average trace in A on a zoomed-in scale, along with an exponential fit (black line) to the initial hyperpolarization. The amplitude and time constant of the exponential fit were 1.55 mV and 132 ms for the example shown; mean values (± SEM) were 2.4 ± 0.3 mV and 173 ± 18 ms (n = 15).

an outwardly rectifying, voltage-dependent open probability under physiological K^+ gradients due to the interaction of permeant ions in the selectivity filter with an activation gate (Schewe et al., 2016). Nonetheless, their rate of activation is fast (millisecond timescale) and voltage-independent, such that they are functionally similar to truly voltage-independent channels with outwardly rectifying single-channel conductance. A primary reason for suspecting K2P channels is that the effects of ultrasound are similar regardless of whether ultrasound is presented 500 ms before or 1 s after the start of the current step (compare Figs. 2 and 3), consistent with the idea that ultrasound affects a channel that does not undergo prolonged voltage-dependent inactivation during sustained depolarizations. Related to this point, the effects of ultrasound are not diminished by repetitive, high-frequency action potential firing (for example, in Fig. 4 C, effects of ultrasound are clearly present throughout the entire 20-Hz, 10-spike train). Further, a striking feature of the effects of ultrasound on spike intervals is that ultrasound always increases the latency to the first spike (Fig. 4, A–C), regardless of the input current and the rate of approach to the initial action potential threshold, consistent with the idea that ultrasound affects a fast-activating, noninactivating channel.

CA1 pyramidal neurons express a variety of K2P channel subunits. Expression of TASK-1 and TASK-3, TREK-1 and TREK-2, TRAAK, and TWIK has been shown at the mRNA level (Talley et al., 2001), while expression at the protein level has been shown for TASK-3 in CA1 pyramidal neurons specifically (Marinc et al., 2014), and for TRAAK throughout the central nervous system (Brohawn et al., 2019). In addition, functional expression of TASK-like currents has been shown in CA1 pyramidal neurons using patch-clamp recording (Taverna et al., 2005). TREK and TRAAK channels are particularly interesting in the present context since they are exceptionally sensitive to mechanical force and to increases in temperature between ∼20 and 40°C (Maingret et al., 2000; Kang et al., 2005). Thus, TREK and TRAAK channels are responsive to the two leading candidate mechanisms by which ultrasound at 43 MHz could modulate ion channel activity.

Activation of K2P channels by ultrasound could account for all of the neurophysiological effects of ultrasound described so far: hyperpolarization of resting membrane potential; inhibition of action potential firing in response to near-threshold current injections; and—although this last point may seem counterintuitive—potentiation of action potential firing at high firing frequencies. Hyperpolarization of resting membrane potential by increased outward K^+ current is straightforward, as is the idea that K^+ current can inhibit firing, but K^+ current can also potentiate firing by its effects on action potential repolarization and after-hyperpolarization (AHP). By accelerating the rate of membrane repolarization following the peak of an action potential (thereby reducing action potential width), K^+ current can reduce inactivation of voltage-dependent Na^+ channels during the action potential, and by increasing the depth of the AHP, it can accelerate the voltage-dependent recovery of Na_V channels from inactivation. Both of these effects would tend to increase the population of Na_V channels available for activation in response to depolarizing current and would increase the maximum action potential firing frequency, as we in fact see in response to ultrasound (Figs. 2 and 3). This mechanism is well-known and widespread in neurophysiology, with several K^+ channels, including both K2P channels and voltage-dependent K^+ (K_V) channels, having been shown to facilitate high-frequency firing (Lien and Jonas, 2003; Brickley et al., 2007; Gu et al., 2007; González et al., 2009; Liu and Bean, 2014; Kanda et al., 2019). The idea that the potentiation of firing by ultrasound is due to effects on action potential repolarization and AHP is supported by the results in Fig. 4 C. For neurons firing at an average firing frequency of 20 Hz in the absence of ultrasound, ultrasound increases the latency to the first spike, while it decreases the intervals between all subsequent spikes. The lack of a potentiating effect on the first spike, despite the otherwise strongly potentiating effects of ultrasound, indicates that the potentiating effect acts through a process (such as action potential repolarization and AHP) that occurs after the initiation of the first action potential. The idea that ultrasound can potentiate firing by activating K^+ current makes specific predictions about the effects of ultrasound on action potential waveform: ultrasound should accelerate repolarization, decrease action potential width, and increase the depth of the AHP.

Effects of ultrasound on action potential waveform

To test the idea that potentiation of firing by ultrasound is due to activation of K^+ channels, we examined the effects of ultrasound on action potential waveform in our recordings. The effects of ultrasound on action potential waveform are consistent with the idea that ultrasound facilitates high-frequency firing by accelerating action potential repolarization. Fig. 6, A–F shows the effect of ultrasound applied 500 ms before the start of the current step on action potential width for cells firing at average frequencies of 5, 10, and 20 Hz (ultrasound also had effects on action potential height, although these were less pronounced than the effects on width; effects on height are detailed in Fig. S3). Ultrasound decreased action potential width for every action potential at all firing frequencies. As shown in Fig. 6, G and H, ultrasound also decreased action potential width when applied 1 s after the start of a current step, again indicating that the channels responsible for these effects continue to influence firing frequency and remain responsive to ultrasound throughout sustained depolarizing current steps.

The effects of ultrasound on action potential width tended to counteract the broadening of action potential width that occurs during high-frequency firing. Fig. 7 plots action potential width as a function of action potential number and input current for the control and ultrasound conditions. In the control condition, there are dramatic differences in width between the first action potential and subsequent action potentials at high input currents, while in the ultrasound condition, these differences are much less pronounced. To quantify this effect, we measured the difference in width between the first and third, first and fifth, and first and last action potentials during the ultrasound stimulus, in response to a +450 pA current step for the control and ultrasound conditions. These differences (mean ± SEM, control versus ultrasound, $n = 9$) were 2.6 ± 0.9 versus 0.7 ± 0.1 ms, 1.5 ±

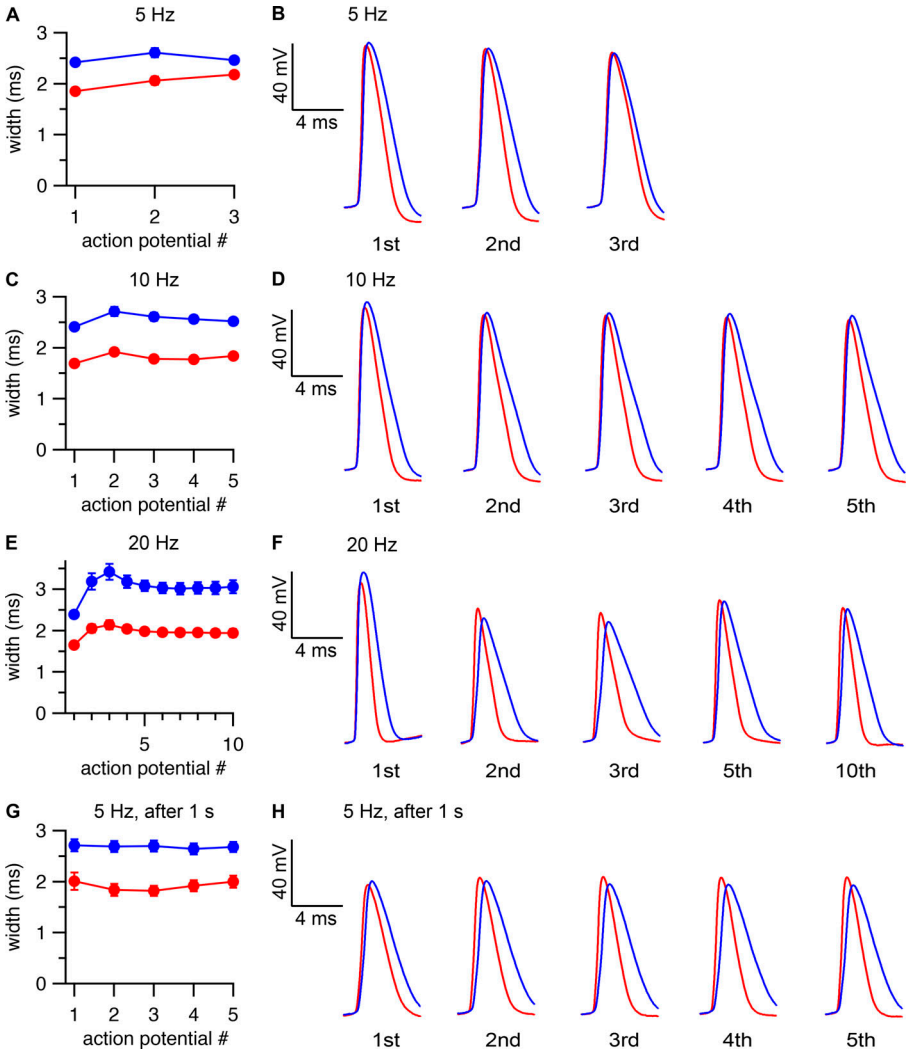

Figure 6. **Ultrasound decreases action potential width. (A and B)** Mean (± SEM, *n* = 13 cells) action potential widths (A) and example action potential waveforms aligned to the action potential threshold (B) as a function of action potential number in the presence (red) and absence (blue) of a 1-s ultrasound pulse starting 500 ms before the current step, for cells firing at an average firing frequency of ∼5 Hz (as measured during the first 500 ms of the current step) in the control condition. **(C and D)** As in A and B, but for cells firing at an average firing frequency of ∼10 Hz in the control condition (*n* = 15). **(E and F)** As in A and B, but for cells firing at an average firing frequency of ∼20 Hz in the control condition (*n* = 13). **(G and H)** As in A and B, but with ultrasound applied 1 s after the start of a 3-s current step, for cells firing at an average firing frequency of ∼5 Hz in the control condition, with firing frequency determined in a 1-s window starting 1 s after the current step (corresponding to the time period of the ultrasound stimulus), and action potential number relative to the start of the ultrasound stimulus (*n* = 6).

0.1 versus 0.5 ± 0.1 ms, and 1.2 ± 0.2 versus 0.5 ± 0.1 ms for the third, fifth, and last action potentials (P = 0.064, 1.4×10^{-5}, and 0.0013, using paired, two-tailed Student's *t* tests). One plausible interpretation of this result is that K2P channels activated by ultrasound cause the membrane voltage during the action potential to repolarize before slower-activating K_V channels, which would otherwise contribute to action potential repolarization, are activated. Since time-dependent activation and inactivation of K_V channels cause action potential broadening during repetitive firing (Giese et al., 1998; Shao et al., 1999; Yue and Yaari, 2004; Kim et al., 2005; Gu et al., 2007), an increase in the contribution of K2P channels lacking time-dependent inactivation with a concomitant decrease in the contribution of K_V channels to action potential repolarization would reduce time- and frequency-dependent action potential broadening.

Although the effects of ultrasound on action potential widths are predominantly due to acceleration of the repolarization phase, we also noted effects on the rising phase of the action potential. These effects are readily apparent in the first derivative of membrane voltage during the action potential (Fig. 8 A) or in action potential phase plots (plots of the first derivative of voltage versus voltage; Fig. 8 B). In fact, the maximum rates of voltage rise and fall during the action potential were both consistently increased by ultrasound throughout a spike train (Fig. 8, C and D). The effect on the falling phase is to be expected based on the observed decrease in spike width and the hypothesis that ultrasound activates K2P channels. The effect on the rising phase is also consistent with this hypothesis, as activation of K2P channels leading to reduced Na_V channel inactivation would increase the number of Na_V channels available to activate during the rising phase of the action potential. Alternatively, increased K2P conductance could increase the rate of action potential rise by decreasing the membrane time constant (Brickley et al., 2007). Consistent with these results, decreases in the rates of action potential rise and fall were seen with knockouts of K2P channels in cerebellar granule neurons (Brickley et al., 2007) and hypothalamic hypocretin/orestin neurons (González et al., 2009), while in a heterologous action potential firing model, higher levels of K2P expression increased the rate of action potential rise (MacKenzie et al., 2015).

In addition to effects of ultrasound on the rising and falling phases of the action potential, we also found effects on the AHP. To quantify these effects, we measured the voltage minimum between action potentials during repetitive firing. Because

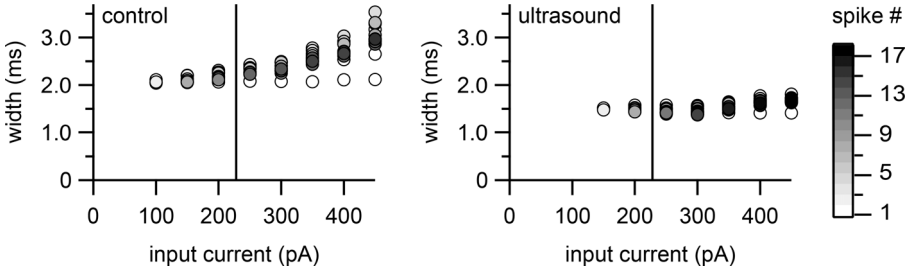

Figure 7. **Ultrasound reduces action potential broadening.** Example data showing action potential width as a function of action potential number (indicated in grayscale, scale bar at far left) and input current level, for the first 500 ms of the current step, for currents from 0 to +450 pA in 50 pA steps, with (right) or without (left) a 1-s ultrasound pulse starting 500 ms before the current step. The vertical lines indicate the approximate location of the transition between inhibitory and potentiating effects of ultrasound.

measurements of this parameter are very sensitive to changes in resting membrane voltage and series resistance that can occur over long recording times, we compared voltage minimums before, during, and after ultrasound application within the same voltage trace (Fig. 9, A and B) and made a similar comparison for control recordings. We performed these comparisons for ultrasound applied 1 s after the start of a current step, for cells firing at an average frequency of 5 Hz in the control condition. This firing frequency is near the transition region between the inhibitory and potentiating effects of ultrasound on spike frequency, such that the spike frequency is similar for the control and ultrasound conditions, allowing us to compare a similar number of interspike voltage minima for the control and ultrasound conditions (Fig. 9 C). This analysis demonstrates that the depth of the AHP is greater during the ultrasound application than before or after it, or during the same time windows for the control condition. Together with the effects of ultrasound on spike waveform (Fig. 6), this result supports the idea that ultrasound activates a sustained outward current, which limits Na_V channel inactivation and thereby potentiates high-frequency firing. Removal of Na_V channel inactivation by membrane hyperpolarization also explains how ultrasound can rescue spiking in neurons that have entered a refractory state due to accumulation of Na_V channel inactivation (Fig. 3 C, bottom right).

Physical mechanism of neuromodulation by high-frequency ultrasound

The idea that ultrasound acts on K2P channels is also consistent with the physical effects of ultrasound on biological tissue. At 43 MHz, two plausible mechanisms through which ultrasound might modulate the activity of ion channels are heating and mechanical stress due to acoustic radiation force. Absorption of acoustic energy by biological tissue as heat can increase its temperature, with effects on ion channel gating and all other biological reactions. Absorption also results in attenuation of ultrasound intensity as the wave propagates, creating spatial gradients in intensity that give rise to radiation force, which in turn produces tissue displacement and strain. At the microscopic scale, this displacement and strain may involve increased tension in the cell membrane, cytoskeleton, and extracellular matrix, all of which may affect excitability through mechanical effects on ion channel proteins. Among the K2P channels that may be expressed by CA1 pyramidal cells, TREK and TRAAK channels are especially sensitive to thermal and mechanical stimuli.

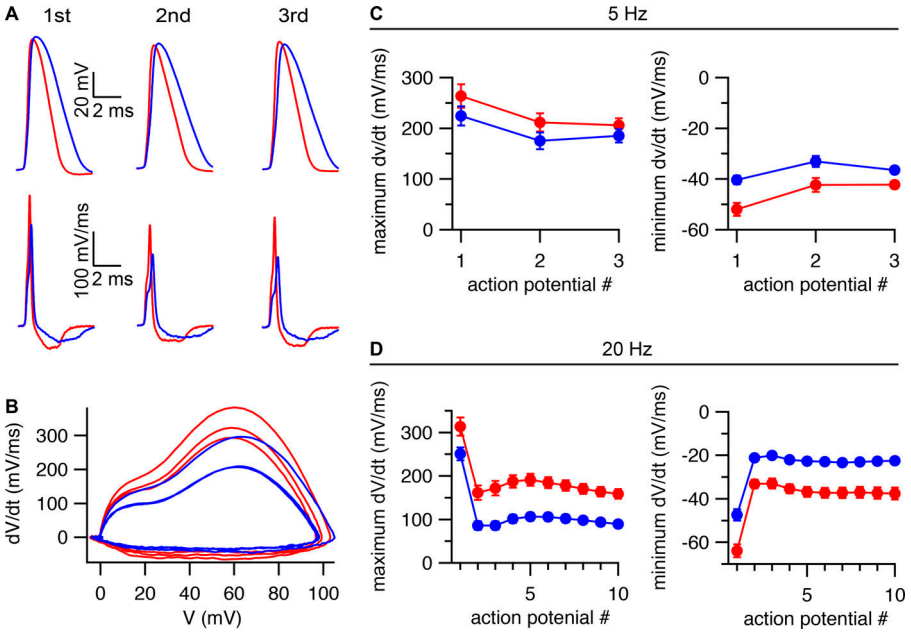

Figure 8. **Effects of ultrasound on depolarization and repolarization rates. (A)** Example traces showing the membrane voltage (top) and its first derivative (bottom) for the first three action potentials in response to a +100-pA current step in the presence (red) and absence (blue) of a 1-s ultrasound pulse starting 500 ms before the current step, aligned to the action potential threshold. **(B)** Phase plots for the action potentials shown in A. **(C and D)** Maximum rates of depolarization (left) and repolarization (right) during the action potential (mean ± SEM, n = 13 cells), as a function of action potential number, in the presence (red) and absence (blue) of a 1-s ultrasound pulse starting 500 ms before the current step, for cells firing at an average firing frequency of 5 Hz (C) or 20 Hz (D) in the control condition.

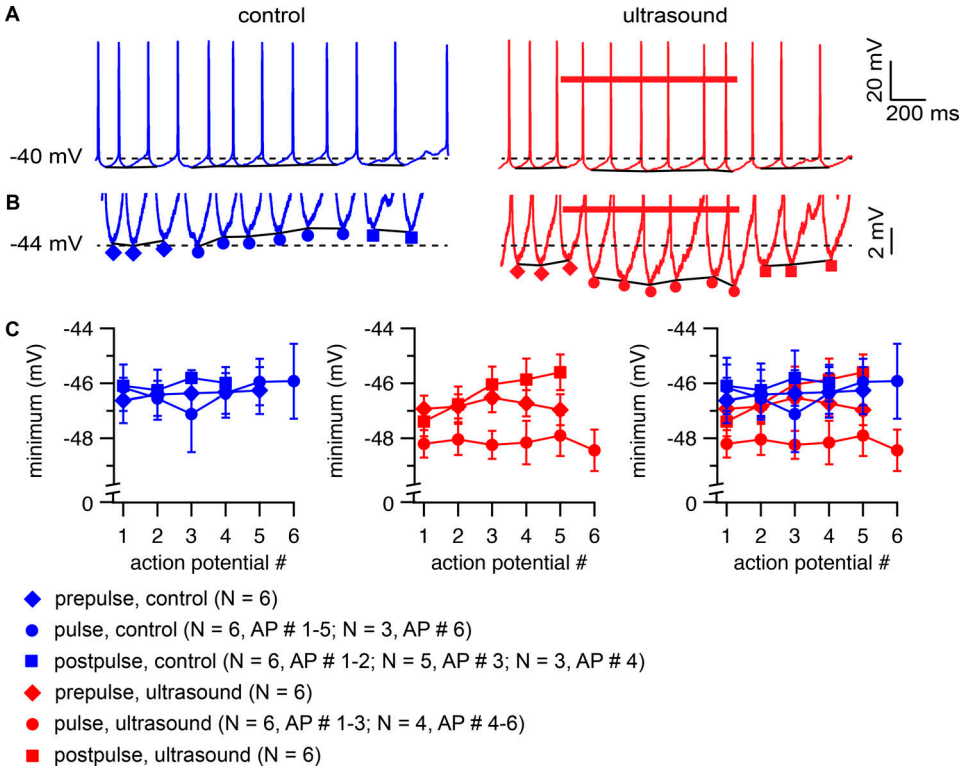

Figure 9. **Ultrasound increases the depth of the AHP. (A)** Example voltage traces comparing voltage minima between action potentials in response to a 3-s, 250-pA current step with (red voltage trace, right) and without (blue voltage trace, left) a 1-s ultrasound pulse (red bar) starting 1 s after the start of the current step. The solid black lines connect the voltage minima between action potentials before, during, or after the ultrasound pulse, or during the corresponding time periods for the control condition. The dashed lines indicate a reference voltage level of −40 mV. The resting membrane voltage for this cell was −63 mV. **(B)** Same as A, on a zoomed-in voltage scale. The red diamonds indicate voltage minima before the ultrasound pulse, red circles indicate voltage minima during the ultrasound pulse, and red squares indicate voltage minima following the ultrasound pulse; blue symbols indicate voltage minima for the corresponding time periods for the control condition. The dashed lines indicate a reference voltage level of −44 mV. **(C)** Mean (± SEM, *n* = 3–6 cells; see figure panel for details) values of the voltage minimum, as a function of action potential (AP) number for the first four to six action potentials before, during, and after the ultrasound pulse, along with the equivalent mean values for the control condition, following the symbolism indicated in B. The means were determined for cells firing at the same average frequency (5 Hz) during a 1-s window starting 1 s after the start of the current step (corresponding to the period of the ultrasound stimulus) in the control condition. For clarity, the results are shown separately for the control group only (left), for the ultrasound group only (middle), and for both groups simultaneously (right). Significant differences between groups were only found in the presence of ultrasound ($P = 1.0 \times 10^{-4}$, 1.4×10^{-5}, and 0.16 for before versus during, during versus after, and before versus after the ultrasound pulse; P = 0.92, 0.39, and 0.35 for comparisons of the same time periods in the control condition; unpaired, two-tailed Student's *t* tests, unequal variance).

To gain further insight into these physical mechanisms, we performed finite-element simulations of the effects of ultrasound on brain slices in the context of our experimental setup. The simulated spatial profiles of ultrasound-induced heating and macroscopic tissue displacement in response to radiation force are shown in Fig. 10, A and B. Notably, the spatial profiles of heating and displacement effects are significantly wider than the 90-micron diameter of the focal volume of the ultrasound beam, with significant heating and displacement occurring several hundreds of microns away from the beam axis (Fig. 10 C). This is an important result because the thermo- and mechanosensitive K2P channels TREK-1 and TRAAK are expressed at high density at the nodes of Ranvier of vertebrate neurons (Brohawn et al., 2019; Kanda et al., 2019). The first node of Ranvier is located ∼100 microns from the axon initial segment (Kole, 2011). In our experiments, the soma of the patched neuron is located approximately on the axis of the ultrasound beam (see Materials and methods), so the first node of Ranvier is probably within the region of the tissue exposed to thermal and mechanical effects of ultrasound. Axonal K^+ channels play important roles in regulating excitability (Shah et al., 2008; Kole, 2011; Kanda et al., 2019). It is therefore plausible that a subpopulation of TREK-1 or TRAAK channels at the nodes of Ranvier could contribute to the neurophysiological effects of ultrasound. The magnitude of the temperature change is also consistent with a thermal mechanism for the effects of ultrasound. The maximum temperature change in the simulation is 1.3°C; temperature changes of this size have previously been shown to affect neural excitability (Owen et al., 2019). The maximum value of the simulated displacement (1.7 microns) is similar to the displacement measured in the retina during ultrasound neuromodulation with stimulus parameters similar to those used here (Menz et al., 2019).

Since the activity of TREK and TRAAK channels is highly temperature-sensitive, we considered whether our results might represent an artifact due to the experiments being

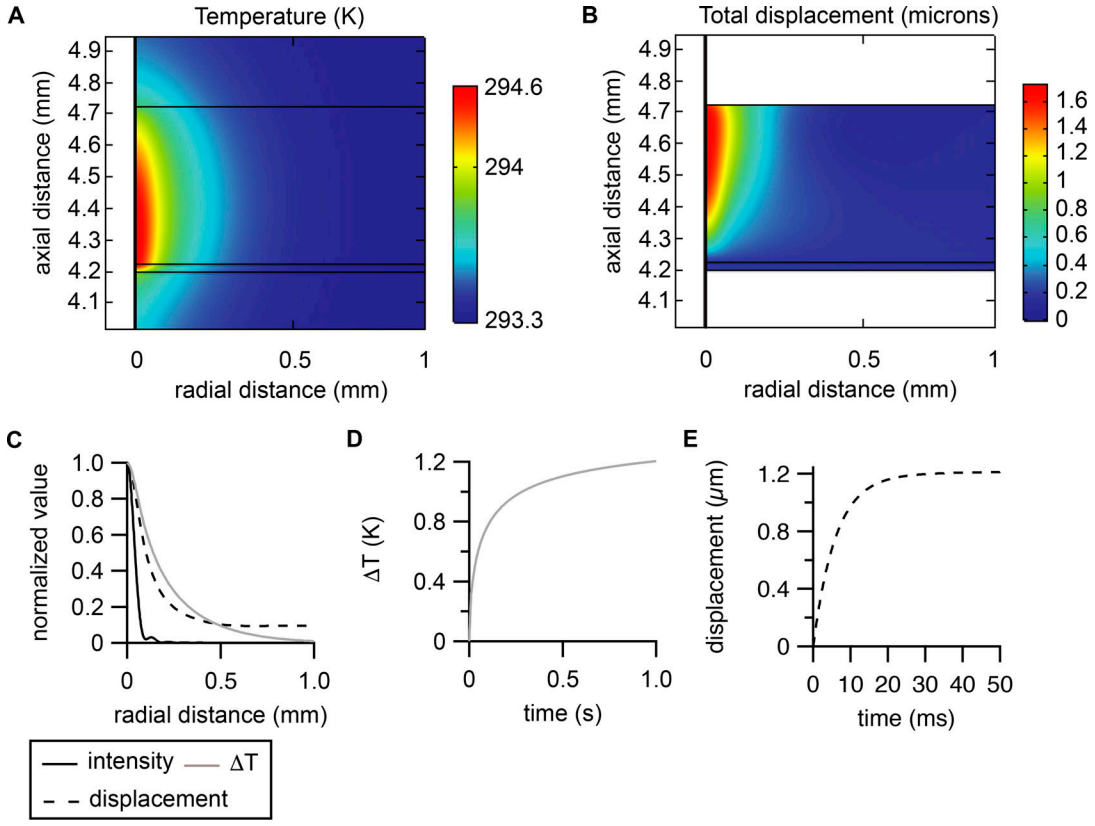

Figure 10. **Simulated tissue heating and displacement in response to ultrasound. (A)** Spatial profile of temperature after 1 s of ultrasound exposure at 43 MHz and 50 W/cm^2, as a function of axial distance from the transducer surface and radial distance from the ultrasound beam axis, in a 500-micron-thick brain slice and 25-micron-thick polystyrene film (middle two layers) and the surrounding fluid (external solution, top layer; and distilled water, bottom layer). **(B)** Spatial profile of the static total displacement in response to acoustic radiation force in the brain slice and polystyrene film. **(C)** Normalized values of the acoustic intensity (solid black line), temperature rise after 1 s of ultrasound exposure (solid gray line) and total displacement (dashed line) at a depth of 250 microns in the brain slice, as a function of radial distance. **(D)** Time course of the temperature rise in response to ultrasound at a depth of 250 microns in the brain slice on the axis of the ultrasound beam. The time course of the temperature change can be described by two exponential components with amplitudes and time constants of −0.56°C and 30 ms, and −0.57°C and 295 ms, for a weighted time constant of 164 ms. **(E)** Time course of the displacement in response at ultrasound at a depth of 250 microns in the brain slice on the axis of the ultrasound beam. The time course of the displacement change can be described by two exponential components with amplitudes and time constants of −1.2 microns and 6 ms, and −0.13 microns and 344 ms, for a weighted time constant of 39 ms. Note that the steady-state displacement is slightly smaller than in the static displacement simulation due to the inclusion of the fluid loading in the dynamic displacement simulation.

performed at room temperature (21–23°C). Room temperature is near the threshold for temperature activation of these channels, such that they are mainly inactive in the absence of other stimuli such as membrane tension, lipid agonists, or acidic pH (Maingret et al., 2000; Kang et al., 2005). Thus, at room temperature in the absence of additional gating stimuli, the relative increase in thermosensitive K2P current would be greater in our experiments than at physiological temperatures, which might lead us to overestimate the importance of K2P channels in the response to ultrasound. On the other hand, the midpoints of the temperature activation curves for TREK and TRAAK channels are near 37°C (in other words, near body temperature in mammals) so that the absolute increase in K2P current in response to increased temperature is near maximal at physiological temperatures, so we might instead be underestimating the thermal effects of ultrasound on K2P channels that would occur in physiological contexts. To cut through this speculation and address these issues, we repeated our experiments measuring the neurophysiological effects of ultrasound in cells firing at a spike frequency of ∼5 Hz at near-physiological temperature (30°C; Fig. S4). Similar to what we observed at room temperature, ultrasound inhibited action potential firing at this relatively low spike frequency and decreased action potential width, indicating that these effects are not especially sensitive to the ambient temperature. However, the hyperpolarizing effect of ultrasound on the resting membrane voltage that we observed at room temperature was no longer apparent at 30°C, possibly due to increased noise in the baseline voltage or more hyperpolarized (in other words, closer to the K^+ reversal potential) resting voltage at higher temperature.

It is instructive to consider the amplitude and time course of the membrane capacitance change in response to ultrasound (Fig. 5) in the context of possible thermal and mechanical mechanisms. As described above (see Effects of ultrasound on resting membrane potential), the capacitance change in response to ultrasound is fast relative to the membrane time

constant, so we can assume that the total charge on the membrane is constant during the initial transient depolarization in response to ultrasound (Fig. 5 A, left arrow). In other words, the numerator in the equation V = Q/C is constant, so for small changes in voltage, the relative change in voltage is approximately inversely proportional to the relative change in capacitance. Empirically, membrane capacitance increases by ∼1% per degree Celsius (Taylor, 1965). This is consistent with the size of the simulated temperature rise (peak simulated temperature rise of 1.3°C compared with the measured amplitude of the initial decrease in voltage of 0.7 ± 0.1%). However, the time course of the temperature rise (Fig. 10 D) is much slower than the time course of the voltage transient (which again, assuming constant Q, is identical to the time course of the capacitance change). The time course of the change in resting membrane potential (173 ± 18 ms; Fig. 5), however, parallels that of the temperature rise (A capacitance change on the time course of the simulated temperature rise would not have a significant effect on the membrane voltage, as it would be counteracted by ionic currents). Thus, the simulated ultrasound heating results strongly suggest that ultrasound affects action potential firing in our experiments at least in part through a thermal effect on ion channels, but do not explain the presence of the capacitive transients.

We considered whether the time course of the capacitive transients could instead be explained by the dynamics of the tissue mechanical response to acoustic radiation force. We sought to determine whether, having already modeled the static displacement of the tissue, we could, without retroactively changing any of the tissue material properties, obtain a time course for tissue displacement similar to that of the capacitive transients using a simple viscoelastic model with reasonable tissue viscous properties (see Materials and methods). We found that this could be achieved using a shear viscosity (μ) of 1 Pa · s (Fig. 10 E). Since the tissue is essentially incompressible in our model (Poisson's ratio [ν] = 0.4998), this is equivalent to a relaxation time of $2\mu \cdot (1 + \nu)/E$ = 6 ms (where E is Young's modulus). Biological tissue is a highly heterogeneous material that displays a variety of active and passive mechanical responses to force, spanning time scales from milliseconds to hours (Ricca et al., 2013), and as a result, its viscous properties are highly sensitive to the time scale of the measurement, and even complex viscoelastic models encompassing multiple relaxation times may not fully describe the viscoelastic behavior of tissue. Nonetheless, the shear viscosity/relaxation time in our model is reasonable for a soft, gel-like material, and is comparable to fast relaxation times observed experimentally in brain tissue (Arbogast and Margulies, 1999; Abolfathi et al., 2009; Rashid et al., 2012, 2013). Moreover, the simulated time course of displacement is consistent with experimental measurements of the tissue displacement in response to ultrasound at 43 MHz and 40 W/cm^2 in the salamander retina, which was found to be complete in <10 ms (Menz et al., 2019).

We can therefore make the reasonable assumption that the capacitive transients are due to a mechanical effect on membrane properties, and we can estimate the size of the potential ion channel gating effects that would occur as a result of this mechanical effect. The capacitance of a lipid bilayer membrane is given by $C = \varepsilon \cdot \varepsilon_0 \cdot A/L$, where ε is the dielectric constant of the hydrophobic core of the lipid bilayer, ε_0 is the permittivity (polarizability) of free space, A is membrane area, and L is the thickness of the hydrophobic core of the membrane. For small strains like those under consideration here, lipid bilayer membranes can be considered incompressible, such that a 1% increase in capacitance corresponds to a 0.5% increase in area and a 0.5% decrease in thickness (White and Thompson, 1973; Alvarez and Latorre, 1978). An increase in membrane area can be converted to an increase in membrane tension (γ) according to $\gamma = \Delta A \cdot K_A$, where ΔA is the relative change in area and K_A is the area elastic constant of the membrane. Area elastic constants measured for lipid membranes are on the order of hundreds of milliNewtons per meter (Evans et al., 1976; Kwok and Evans, 1981; Needham and Nunn, 1990). If the capacitive transients are due to membrane strain, the resulting membrane tension is on the order of a few 0.1 mN/m to a few mN/m. These values are similar to the tension thresholds for activation of mechanosensitive K2P channels (estimated as 0.5–4 mN/m for activation of TREK-1 and TRAAK; Brohawn et al., 2014), which are low relative to other known mammalian mechanosensitive channels. Notably, a recent in vivo ultrasound neuromodulation study of the murine sciatic nerve at 4 MHz found that tissue displacement in vivo was highly correlated with the neuromodulation effects (Lee et al., 2020). Nonetheless, additional data or theoretical advances would be required to firmly associate these capacitive transients with changes in membrane tension. If such an association could be made, it would provide strong evidence that ultrasound modulates action potential firing through mechanical effects of radiation force in our experiments. At present, our results do not rule out this idea, but the case for mechanical effects remains speculative, while the role of thermal effects seems highly plausible. Nonetheless, our simulation results support the conclusion that both inhibitory and excitatory effects of high-frequency ultrasound on action potential firing are due to activation of thermo- and mechanosensitive K2P channels.

Discussion

To summarize, the neurophysiological effects of ultrasound that we have described here can all be explained by activation of a sustained outward current. We argue that the molecular basis of this outward current is most likely one or more of the K2P channels expressed by CA1 pyramidal neurons. Although a variety of K_V currents shape the action potential waveform and regulate excitability in these neurons, several arguments suggest that K2P channels are the molecular basis of the ultrasound-activated outward conductance. First, the K2P channels TREK and TRAAK, being strongly mechanosensitive and thermosensitive, have biophysical properties that make them especially sensitive to the physical effects of ultrasound. Second, the fact that ultrasound has similar effects on firing frequency whether it is applied 500 ms before or 1 s after the start of a current step suggests that ultrasound affects firing through a channel that does not undergo prolonged voltage-dependent inactivation during sustained depolarizations. Finally, the neurophysiological

effects of ultrasound are, strikingly, essentially the opposite of those caused by knock-out of K2P channels in other neurons, as detailed in the following paragraph.

Knock-out of TASK-3 channels in cerebellar granule neurons increased excitability at low input currents, but decreased excitability at high-input currents and led to failure of sustained high-frequency firing (Brickley et al., 2007). In addition, knock-out of TASK-3 decreased the maximum firing frequency and decreased action potential height while increasing action potential width through a decrease in the rates of both action potential rise and fall. Similarly, double knock-out of TASK-1 and TASK-3 in hypothalamic hypocretin/orexin neurons inhibited high-frequency action potential firing, reduced the rates of action potential rise and fall, and decreased the depth of the AHP (González et al., 2009). The connection between our results and these knock-out studies is supported by experiments in a heterologous model system consisting of human embryonic kidney cells transfected with TREK-1 and TASK-3 (with endogenous K_V channels blocked) and Na_V channels simulated by dynamic clamp (MacKenzie et al., 2015). In this model system, high levels of K2P expression were necessary for repetitive action potential firing, and increased K2P conductance increased the rates of action potential rise and fall and increased the threshold current for action potential firing (In the context of this model system, a 74% potentiation of the K2P conductance by halothane produced effects on the rates of rise and fall of the same order as we see here, potentially providing an estimate of the potentiation of K2P conductance by ultrasound in our experiments. However, caution should be used in extrapolating from this heterologous model system to neurons expressing a considerably more complex array of ion channels). Finally, TREK-1 and TRAAK channels are also necessary for high-frequency firing at the nodes of Ranvier of afferent neurons (Kanda et al., 2019).

Ultrasound neuromodulation has been studied in vertebrate axon preparations, where it has generally been found that ultrasound inhibits action potential conduction, with the effect specifically attributed to heating in some cases (Young and Henneman, 1961; Mihran et al., 1990; Tsui et al., 2005; Colucci et al., 2009). These results are consistent with the idea that activation of K2P channels by ultrasound can inhibit action potential firing, but it would be worthwhile to revisit these experiments to see whether the bidirectional, spike frequency–dependent effect that we observe is also present in such preparations. Our results also suggest an approach to ultrasound neuromodulation in which action potential propagation is the locus of neuromodulation, targeting white-matter tracts instead of soma-dense gray matter. The idea that ultrasound-activated K^+ currents can both inhibit and potentiate firing might also help explain why ultrasound can both inhibit and potentiate neural activity in vivo (Min et al., 2011).

Although activation of K2P channels is sufficient to explain our results, we do not rule out the possibility that ultrasound affects other channels in addition to K2P channels; indeed, we think it is likely that ultrasound does affect other channels to some extent. All ion channel gating reactions are sensitive to temperature, with typical Q10 (temperature coefficient) values of ∼3, such that their rates would be expected to increase by ∼10% based on the temperature changes in our simulations (Hille, 2001). Mechanical effects of radiation force could also affect channels besides K2P channels. The mechanically gated channel Piezo2 is expressed in a subset of CA1 pyramidal neurons (Wang and Hamill, 2020). Piezo1 (Qiu et al., 2019) and TRP (transient receptor potential) channels (Oh et al., 2020; Yoo et al., 2020) have been experimentally linked to ultrasound neuromodulation effects. In addition, most ion channels and membrane proteins, while not functioning physiologically as mechanoreceptors, are sensitive to mechanical stimuli to some extent, either through the energetics of their interactions with the hydrophobic core of the lipid bilayer or through mechanical interactions with the cytoskeleton or extracellular matrix. In fact, gating of voltage-dependent Na^+ (Morris and Juranka, 2007), K^+ (Tabarean and Morris, 2002; Laitko and Morris, 2004; Beyder et al., 2010), and Ca^{2+} (Calabrese et al., 2002) channels, and of NMDA receptor channels (Kloda et al., 2007), can be modulated by membrane stretch in membrane patches. However, we previously were unable to detect any mechanical modulation of heterologously expressed $Na_V1.2$ channels by ultrasound at 43 MHz and 90 W/cm^2 under conditions where ultrasound activated the mammalian mechanoreceptor channel Piezo1 (Prieto et al., 2018). Neural Na_V channels and potassium channels of the K_V7 family interact with the periodic actin cytoskeleton of axons through spectrin and ankyrin-G at the axon initial segment and nodes of Ranvier (Zhou et al., 1998; Pan et al., 2006; Leterrier, 2018), suggesting that they may be sensitive to modulation by cytoskeletal tension due to acoustic radiation force. The concentrations of TREK-1 and TRAAK channels at the nodes of Ranvier suggest that some similar interaction with the cytoskeleton may be involved in the localization of these channels, although this has not been demonstrated, and the intracellular domains that would facilitate such interactions are relatively small in K2P channels. Ultrasound has been shown to cause changes in cytoskeletal structure (Mizrahi et al., 2012), which might also affect the activity of cytoskeleton-associated channels. Thus, investigation of the role of other ion channels in ultrasound neuromodulation should continue. Notably, several of the channels discussed above have roles in synaptic transmission, so effects of ultrasound on these channels would not be revealed by our experiments on somatic excitability in response to injected current.

It is well established that high-intensity light at infrared and shorter wavelengths can modulate neural activity through tissue heating. As a general principle, thermal neuromodulation effects in response to optical stimulation would be expected to be very similar to thermal neuromodulation effects caused by ultrasound, and studies of optical neuromodulation could therefore provide useful guidance in interpreting our results. However, optically based thermal neuromodulation experiments are highly heterogeneous in terms of the neuromodulation effect, the temperature rise required to produce the effect, and the mechanistic interpretation of the results (Wells et al., 2007; Richter et al., 2011; Shapiro et al., 2012; Duke et al., 2013; Walsh et al., 2016; Lothet et al., 2017; Paris et al., 2017; Owen et al., 2019; Zhu et al., 2019), so their usefulness is limited in this respect. Both inhibition and potentiation of firing have been reported,

and the increase in temperature has varied considerably, ranging from <1°C to tens of degrees Celsius. The temperature rise in our simulations is on the low end of this range. However, it has been proposed that spatial or temporal gradients in temperature, rather than the absolute temperature change, may determine the response to thermal stimuli (Wells et al., 2007; Paris et al., 2017). In addition, heating can cause phase changes in lipid bilayers, which have been shown to modulate ion channel activity (Seeger et al., 2010); in this case, the response to heating would also depend critically on the initial temperature. Interestingly, a recent study demonstrated inhibition of firing by small (2°C or less) increases in temperature in several different types of neurons, but not in CA1 pyramidal neurons (Owen et al., 2019). These effects were attributed to inward rectifier potassium channels, which are not expressed in CA1 pyramidal neurons. However, our results suggest that the lack of an effect in pyramidal neurons could also be explained if the experiments were performed at a point on the f-i curve where competing inhibitory and excitatory effects of heat-activated K^+ current result in no net effect on firing frequency. A recent in vivo ultrasound neuromodulation study in a rat model using ultrasound at 3.2 MHz with exceptionally long ultrasound exposure times (tens of seconds; see below for a more general discussion of in vivo ultrasound neuromodulation studies) also found that inhibition could be produced by ultrasound-induced temperature rises of 2°C or less (Darrow et al., 2019), consistent with this result and our results.

Finally, a critical question—to which we cannot yet provide a definitive answer—is whether the mechanisms underlying the neuromodulatory effects of ultrasound are the same in our experiments and in in vivo experiments using low frequencies. Two results that strongly argue against similar mechanisms are the much lower intensities that have been reported to cause neuromodulatory effects in some low-frequency, in vivo experiments in small animal models (Tufail et al., 2010) as compared with our results, and the apparent increase in efficacy of ultrasound neuromodulation at lower frequencies in in vivo experiments. Both thermal and radiation force effects are proportional to ultrasound intensity, and to the ultrasound attenuation coefficient, which in tissue is proportional to frequency raised to the power of ~1.1 (Hand, 1998), so these effects would generally be smaller in in vivo experiments (especially small animal experiments) as compared with our experiments. Compounding this issue is the fact that opposite dependences on the ultrasound frequency have been observed in in vivo and in vitro experiments. In an in vivo mouse model of ultrasound neuromodulation, it was determined that the efficacy of neuromodulation decreased with increasing frequency over the range 0.25–2.9 MHz (King et al., 2013; Ye et al., 2016). This frequency dependence is the opposite of what would be expected for either a thermal or radiation force mechanism. In contrast, Menz et al. (2019) found that the efficacy of neuromodulation increases with frequency over the range 1.9–43 MHz in the retina in vitro, a thin neural tissue preparation similar to the one used in our experiments. However, they proposed a model to explain this discrepancy. Lower ultrasound frequencies generally result in a larger stimulated tissue volume, which could translate into a more effective stimulus for certain structures of circuit-level neural connectivity, despite a weaker effect of low-frequency ultrasound at the level of an individual cell (The model was presented in the context of a radiation force mechanism, but the same principle could apply for a thermal mechanism). The idea that circuit-level mechanisms can amplify the response to ultrasound is supported by comparison of our results with the response to ultrasound in the retina at 43 MHz. In the retina, potentiation of action potential firing by ultrasound at 43 MHz saturates at 10 W/cm^2, as measured at the population level in an intact, active neural circuit. Although we have not performed a detailed investigation of the intensity dependence, we find that a much higher intensity, 50 W/cm^2, produces relatively moderate effects on excitability in single cells in the absence of significant network activity. Focusing solely on the local, cell-level amplitude of thermal and radiation force effects may therefore overlook important factors related to the global, network-level distribution of these effects. Such considerations may eliminate the differences in effective ultrasound parameters for in vivo and in vitro experiments as an argument against similar physical mechanisms for neuromodulation by high- and low-frequency ultrasound.

In conclusion, our results demonstrate that high-frequency ultrasound is a viable and promising modality for neuromodulation applications where frequency is not limited by transmission through the skull, and our insights into the common molecular mechanisms underlying both inhibitory and excitatory effects of high-frequency ultrasound pave the way for rational design and optimization of neuromodulation protocols to consistently produce either inhibitory or excitatory effects.

Acknowledgments

Olaf S. Andersen served as editor.

We thank the principal investigators and members of the Baccus, Butts-Pauly, and Huguenard laboratories for helpful discussions. We thank Mike Menz and Stephen Baccus for critically reading the manuscript. We thank Marianna Kiraly, Dong Li, and Jason Clark for help with hippocampal slice preparation and recording. We thank the Stephen Boxer laboratory (Department of Chemistry, Stanford University, Stanford, CA) for sharing their plasma cleaner.

This work was supported by National Institutes of Health grant R01 EB019005 (to M. Maduke and B. Khuri-Yakub) and National Institutes of Health Brain Research through Advancing Innovative Neurotechnologies (BRAIN) initiative R01 NS11215 (to M. Maduke and B. Khuri-Yakub) and by the Mathers Foundation (to M. Maduke) and grant MH111768 (to D. Madison).

The authors declare no competing financial interests.

Author contributions: M.L. Prieto performed experiments, analyzed data, and wrote the manuscript. M.L. Prieto and K. Firouzi performed computational modeling. M. Maduke, D.V. Madison, and B.T. Khuri-Yakub supervised research. All authors contributed to the design and interpretation of experiments and edited and revised the manuscript.

Submitted: 2 June 2020
Accepted: 14 September 2020

References

Abolfathi, N., A. Naik, M. Sotudeh Chafi, G. Karami, and M. Ziejewski. 2009. A micromechanical procedure for modelling the anisotropic mechanical properties of brain white matter. *Comput. Methods Biomech. Biomed. Engin.* 12:249–262. https://doi.org/10.1080/10255840802430587

Alvarez, O., and R. Latorre. 1978. Voltage-dependent capacitance in lipid bilayers made from monolayers. *Biophys. J.* 21:1–17. https://doi.org/10.1016/S0006-3495(78)85505-2

Arbogast, K.B., and S.S. Margulies. 1999. A fiber-reinforced composite model of the viscoelastic behavior of the brainstem in shear. *J. Biomech.* 32: 865–870. https://doi.org/10.1016/S0021-9290(99)00042-1

Bean, B.P. 2007. The action potential in mammalian central neurons. *Nat. Rev. Neurosci.* 8:451–465. https://doi.org/10.1038/nrn2148

Beyder, A., J.L. Rae, C. Bernard, P.R. Strege, F. Sachs, and G. Farrugia. 2010. Mechanosensitivity of Nav1.5, a voltage-sensitive sodium channel. *J. Physiol.* 588:4969–4985. https://doi.org/10.1113/jphysiol.2010.199034

Blackmore, J., S. Shrivastava, J. Sallet, C.R. Butler, and R.O. Cleveland. 2019. Ultrasound Neuromodulation: A Review of Results, Mechanisms and Safety. *Ultrasound Med. Biol.* 45:1509–1536. https://doi.org/10.1016/j.ultrasmedbio.2018.12.015

Blanton, M.G., J.J. Lo Turco, and A.R. Kriegstein. 1989. Whole cell recording from neurons in slices of reptilian and mammalian cerebral cortex. *J. Neurosci. Methods.* 30:203–210. https://doi.org/10.1016/0165-0270(89)90131-3

Brickley, S.G., M.I. Aller, C. Sandu, E.L. Veale, F.G. Alder, H. Sambi, A. Mathie, and W. Wisden. 2007. TASK-3 two-pore domain potassium channels enable sustained high-frequency firing in cerebellar granule neurons. *J. Neurosci.* 27:9329–9340. https://doi.org/10.1523/JNEUROSCI.1427-07.2007

Brohawn, S.G., Z. Su, and R. MacKinnon. 2014. Mechanosensitivity is mediated directly by the lipid membrane in TRAAK and TREK1 K+ channels. *Proc. Natl. Acad. Sci. USA.* 111:3614–3619. https://doi.org/10.1073/pnas.1320768111

Brohawn, S.G., W. Wang, A. Handler, E.B. Campbell, J.R. Schwarz, and R. MacKinnon. 2019. The mechanosensitive ion channel TRAAK is localized to the mammalian node of Ranvier. *eLife.* 8. e50403. https://doi.org/10.7554/eLife.50403

Bystritsky, A., A.S. Korb, P.K. Douglas, M.S. Cohen, W.P. Melega, A.P. Mulgaonkar, A. DeSalles, B.K. Min, and S.S. Yoo. 2011. A review of low-intensity focused ultrasound pulsation. *Brain Stimul.* 4:125–136. https://doi.org/10.1016/j.brs.2011.03.007

Calabrese, B., I.V. Tabarean, P. Juranka, and C.E. Morris. 2002. Mechanosensitivity of N-type calcium channel currents. *Biophys. J.* 83: 2560–2574. https://doi.org/10.1016/S0006-3495(02)75267-3

Calhoun, M.A., S.A. Bentil, E. Elliott, J.J. Otero, J.O. Winter, and R.B. Dupaix. 2019. Beyond linear elastic modulus: viscoelastic models for brain and brain mimetic hydrogels. *ACS Biomater. Sci. Eng.* 5:3964–3973. https://doi.org/10.1021/acsbiomaterials.8b01390

Castañeda-Castellanos, D.R., A.C. Flint, and A.R. Kriegstein. 2006. Blind patch clamp recordings in embryonic and adult mammalian brain slices. *Nat. Protoc.* 1:532–542. https://doi.org/10.1038/nprot.2006.75

Chemical Rubber Company. 1965. Handbook of Chemistry and Physics. 45th edition. Chemical Rubber Company, Cleveland, OH.

Colucci, V., G. Strichartz, F. Jolesz, N. Vykhodtseva, and K. Hynynen. 2009. Focused ultrasound effects on nerve action potential in vitro. *Ultrasound Med. Biol.* 35:1737–1747. https://doi.org/10.1016/j.ultrasmedbio.2009.05.002

Cotero, V., Y. Fan, T. Tsaava, A.M. Kressel, I. Hancu, P. Fitzgerald, K. Wallace, S. Kaanumalle, J. Graf, W. Rigby, et al. 2019. Noninvasive sub-organ ultrasound stimulation for targeted neuromodulation. *Nat. Commun.* 10: 952. https://doi.org/10.1038/s41467-019-08750-9

Darrow, D.P., P. O'Brien, T.J. Richner, T.I. Netoff, and E.S. Ebbini. 2019. Reversible neuroinhibition by focused ultrasound is mediated by a thermal mechanism. *Brain Stimul.* 12:1439–1447.

de Korte, C.L., A.F. van der Steen, and J.M. Thijssen. 1994. Acoustic velocity and attenuation of eye tissues at 20 MHz. *Ultrasound Med. Biol.* 20: 471–480. https://doi.org/10.1016/0301-5629(94)90102-3

Downs, M.E., S.A. Lee, G. Yang, S. Kim, Q. Wang, and E.E. Konofagou. 2018. Non-invasive peripheral nerve stimulation via focused ultrasound in vivo. *Phys. Med. Biol.* 63. 035011. https://doi.org/10.1088/1361-6560/aa9fc2

Duck, F.A. 1998. Radiation Pressure and Acoustic Streaming. *In* Ultrasound in Medicine. F. Duck, A. Baker, and H. Starritt, editors. Institute of Physics Publishing, Philadelphia, PA. https://doi.org/10.1887/0750305932/b673c3

Duke, A.R., M.W. Jenkins, H. Lu, J.M. McManus, H.J. Chiel, and E.D. Jansen. 2013. Transient and selective suppression of neural activity with infrared light. *Sci. Rep.* 3:2600. https://doi.org/10.1038/srep02600

Evans, E.A., R. Waugh, and L. Melnik. 1976. Elastic area compressibility modulus of red cell membrane. *Biophys. J.* 16:585–595. https://doi.org/10.1016/S0006-3495(76)85713-X

Fomenko, A., C. Neudorfer, R.F. Dallapiazza, S.K. Kalia, and A.M. Lozano. 2018. Low-intensity ultrasound neuromodulation: An overview of mechanisms and emerging human applications. *Brain Stimul.* 11: 1209–1217. https://doi.org/10.1016/j.brs.2018.08.013

Fry, F.J., H.W. Ades, and W.J. Fry. 1958. Production of reversible changes in the central nervous system by ultrasound. *Science.* 127:83–84. https://doi.org/10.1126/science.127.3289.83

Gaur, U., and B. Wunderlich. 1982. Heat-Capacity and Other Thermodynamic Properties of Linear Macromolecules. 5. Polystyrene. *J. Phys. Chem. Ref. Data.* 11:313–325. https://doi.org/10.1063/1.555663

Gavrilov, L.R., E.M. Tsirulnikov, and I.A. Davies. 1996. Application of focused ultrasound for the stimulation of neural structures. *Ultrasound Med. Biol.* 22:179–192. https://doi.org/10.1016/0301-5629(96)83782-3

Giese, K.P., J.F. Storm, D. Reuter, N.B. Fedorov, L.R. Shao, T. Leicher, O. Pongs, and A.J. Silva. 1998. Reduced K+ channel inactivation, spike broadening, and after-hyperpolarization in Kvbeta1.1-deficient mice with impaired learning. *Learn. Mem.* 5:257–273.

González, J.A., L.T. Jensen, S.E. Doyle, M. Miranda-Anaya, M. Menaker, L. Fugger, D.A. Bayliss, and D. Burdakov. 2009. Deletion of TASK1 and TASK3 channels disrupts intrinsic excitability but does not abolish glucose or pH responses of orexin/hypocretin neurons. *Eur. J. Neurosci.* 30:57–64. https://doi.org/10.1111/j.1460-9568.2009.06789.x

Gu, N., K. Vervaeke, and J.F. Storm. 2007. BK potassium channels facilitate high-frequency firing and cause early spike frequency adaptation in rat CA1 hippocampal pyramidal cells. *J. Physiol.* 580:859–882. https://doi.org/10.1113/jphysiol.2006.126367

Hand, J.W. 1998. Ultrasound Hyperthermia and the Prediction of Heating. *In* Ultrasound in Medicine. F. Duck, A. Baker, and H. Starritt, editors. Institute of Physics Publishing, Philadelphia, PA. https://doi.org/10.1887/0750305932/b673c8

Harper, C.A. 2006. Handbook of Plastics Technologies: The Complete Guide to Properties and Performance. McGraw-Hill,, New York, NY.

Hille, B. 2001. Ion Channels of Excitable Membranes. Third edition. Sinauer Associates, Inc., Sunderland, MA.

Kanda, H., J. Ling, S. Tonomura, K. Noguchi, S. Matalon, and J.G. Gu. 2019. TREK-1 and TRAAK Are Principal K^+ Channels at the Nodes of Ranvier for Rapid Action Potential Conduction on Mammalian Myelinated Afferent Nerves. *Neuron.* 104:960–971.e7. https://doi.org/10.1016/j.neuron.2019.08.042

Kang, D., C. Choe, and D. Kim. 2005. Thermosensitivity of the two-pore domain K+ channels TREK-2 and TRAAK. *J. Physiol.* 564:103–116. https://doi.org/10.1113/jphysiol.2004.081059

Khaliq, Z.M., and B.P. Bean. 2010. Pacemaking in dopaminergic ventral tegmental area neurons: depolarizing drive from background and voltage-dependent sodium conductances. *J. Neurosci.* 30:7401–7413. https://doi.org/10.1523/JNEUROSCI.0143-10.2010

Kim, J., D.S. Wei, and D.A. Hoffman. 2005. Kv4 potassium channel subunits control action potential repolarization and frequency-dependent broadening in rat hippocampal CA1 pyramidal neurones. *J. Physiol.* 569:41–57. https://doi.org/10.1113/jphysiol.2005.095042

King, R.L., J.R. Brown, W.T. Newsome, and K.B. Pauly. 2013. Effective parameters for ultrasound-induced in vivo neurostimulation. *Ultrasound Med. Biol.* 39:312–331. https://doi.org/10.1016/j.ultrasmedbio.2012.09.009

Kloda, A., L. Lua, R. Hall, D.J. Adams, and B. Martinac. 2007. Liposome reconstitution and modulation of recombinant N-methyl-D-aspartate receptor channels by membrane stretch. *Proc. Natl. Acad. Sci. USA.* 104: 1540–1545. https://doi.org/10.1073/pnas.0609649104

Kole, M.H. 2011. First node of Ranvier facilitates high-frequency burst encoding. *Neuron.* 71:671–682. https://doi.org/10.1016/j.neuron.2011.06.024

Krasovitski, B., V. Frenkel, S. Shoham, and E. Kimmel. 2011. Intramembrane cavitation as a unifying mechanism for ultrasound-induced bioeffects. *Proc. Natl. Acad. Sci. USA.* 108:3258–3263. https://doi.org/10.1073/pnas.1015771108

Kubanek, J., J. Shi, J. Marsh, D. Chen, C. Deng, and J. Cui. 2016. Ultrasound modulates ion channel currents. *Sci. Rep.* 6:24170. https://doi.org/10.1038/srep24170

Kwok, R., and E. Evans. 1981. Thermoelasticity of large lecithin bilayer vesicles. *Biophys. J.* 35:637–652. https://doi.org/10.1016/S0006-3495(81)84817-5

Laitko, U., and C.E. Morris. 2004. Membrane tension accelerates rate-limiting voltage-dependent activation and slow inactivation steps in a Shaker channel. *J. Gen. Physiol.* 123:135–154. https://doi.org/10.1085/jgp.200308965

Lee, S.A., H.A.S. Kamimura, M.T. Burgess, and E.E. Konofagou. 2020. Displacement imaging for focused ultrasound peripheral nerve neuromodulation. *IEEE Trans. Med. Imaging*. PP.

Leighton, T.G. 1998. An Introduction to Acoustic Cavitation. *In* Ultrasound in Medicine. F. Duck, A. Baker, and H. Starritt, editors. Institute of Physics Publishing, Philadelphia, PA. https://doi.org/10.1887/0750305932/b673c11

Leterrier, C. 2018. The Axon Initial Segment: An Updated Viewpoint. *J. Neurosci.* 38:2135–2145. https://doi.org/10.1523/JNEUROSCI.1922-17.2018

Lien, C.C., and P. Jonas. 2003. Kv3 potassium conductance is necessary and kinetically optimized for high-frequency action potential generation in hippocampal interneurons. *J. Neurosci.* 23:2058–2068. https://doi.org/10.1523/JNEUROSCI.23-06-02058.2003

Liu, P.W., and B.P. Bean. 2014. Kv2 channel regulation of action potential repolarization and firing patterns in superior cervical ganglion neurons and hippocampal CA1 pyramidal neurons. *J. Neurosci.* 34:4991–5002. https://doi.org/10.1523/JNEUROSCI.1925-13.2014

Lothet, E.H., K.M. Shaw, H. Lu, J. Zhuo, Y.T. Wang, S. Gu, D.B. Stolz, E.D. Jansen, C.C. Horn, H.J. Chiel, et al. 2017. Selective inhibition of small-diameter axons using infrared light. *Sci. Rep.* 7:3275. https://doi.org/10.1038/s41598-017-03374-9

MacKenzie, G., N.P. Franks, and S.G. Brickley. 2015. Two-pore domain potassium channels enable action potential generation in the absence of voltage-gated potassium channels. *Pflugers Arch.* 467:989–999. https://doi.org/10.1007/s00424-014-1660-6

Madison, D.V., and R.A. Nicoll. 1984. Control of the repetitive discharge of rat CA 1 pyramidal neurones in vitro. *J. Physiol.* 354:319–331. https://doi.org/10.1113/jphysiol.1984.sp015378

Maingret, F., I. Lauritzen, A.J. Patel, C. Heurteaux, R. Reyes, F. Lesage, M. Lazdunski, and E. Honoré. 2000. TREK-1 is a heat-activated background K(+) channel. *EMBO J.* 19:2483–2491. https://doi.org/10.1093/emboj/19.11.2483

Malinow, R., and R.W. Tsien. 1990. Presynaptic enhancement shown by whole-cell recordings of long-term potentiation in hippocampal slices. *Nature.* 346:177–180. https://doi.org/10.1038/346177a0

Marinc, C., C. Derst, H. Prüss, and R.W. Veh. 2014. Immunocytochemical localization of TASK-3 protein (K2P9.1) in the rat brain. *Cell. Mol. Neurobiol.* 34:61–70. https://doi.org/10.1007/s10571-013-9987-7

Menz, M.D., O. Oralkan, P.T. Khuri-Yakub, and S.A. Baccus. 2013. Precise neural stimulation in the retina using focused ultrasound. *J. Neurosci.* 33:4550–4560. https://doi.org/10.1523/JNEUROSCI.3521-12.2013

Menz, M.D., P. Ye, K. Firouzi, A. Nikoozadeh, K.B. Pauly, P. Khuri-Yakub, and S.A. Baccus. 2019. Radiation Force as a Physical Mechanism for Ultrasonic Neurostimulation of the *Ex Vivo* Retina. *J. Neurosci.* 39:6251–6264. https://doi.org/10.1523/JNEUROSCI.2394-18.2019

Mihran, R.T., F.S. Barnes, and H. Wachtel. 1990. Temporally-specific modification of myelinated axon excitability in vitro following a single ultrasound pulse. *Ultrasound Med. Biol.* 16:297–309. https://doi.org/10.1016/0301-5629(90)90008-Z

Min, B.K., A. Bystritsky, K.I. Jung, K. Fischer, Y. Zhang, L.S. Maeng, S.I. Park, Y.A. Chung, F.A. Jolesz, and S.S. Yoo. 2011. Focused ultrasound-mediated suppression of chemically-induced acute epileptic EEG activity. *BMC Neurosci.* 12:23. https://doi.org/10.1186/1471-2202-12-23

Mizrahi, N., E.H. Zhou, G. Lenormand, R. Krishnan, D. Weihs, J.P. Butler, D.A. Weitz, J.J. Fredberg, and E. Kimmel. 2012. Low intensity ultrasound perturbs cytoskeleton dynamics. *Soft Matter.* 8:2438–2443. https://doi.org/10.1039/c2sm07246g

Morris, C.E., and P.F. Juranka. 2007. Nav channel mechanosensitivity: activation and inactivation accelerate reversibly with stretch. *Biophys. J.* 93:822–833. https://doi.org/10.1529/biophysj.106.101246

Needham, D., and R.S. Nunn. 1990. Elastic deformation and failure of lipid bilayer membranes containing cholesterol. *Biophys. J.* 58:997–1009. https://doi.org/10.1016/S0006-3495(90)82444-9

Oh, S.J., J.M. Lee, H.B. Kim, J. Lee, S. Han, J.Y. Bae, G.S. Hong, W. Koh, J. Kwon, E.S. Hwang, et al. 2020. Ultrasonic Neuromodulation via Astrocytic TRPA1. *Curr. Biol.* 30:948. https://doi.org/10.1016/j.cub.2020.02.042

Owen, S.F., M.H. Liu, and A.C. Kreitzer. 2019. Thermal constraints on in vivo optogenetic manipulations. *Nat. Neurosci.* 22:1061–1065. https://doi.org/10.1038/s41593-019-0422-3

Pan, Z., T. Kao, Z. Horvath, J. Lemos, J.Y. Sul, S.D. Cranstoun, V. Bennett, S.S. Scherer, and E.C. Cooper. 2006. A common ankyrin-G-based mechanism retains KCNQ and NaV channels at electrically active domains of the axon. *J. Neurosci.* 26:2599–2613. https://doi.org/10.1523/JNEUROSCI.4314-05.2006

Paris, L., I. Marc, B. Charlot, M. Dumas, J. Valmier, and F. Bardin. 2017. Millisecond infrared laser pulses depolarize and elicit action potentials on *in-vitro* dorsal root ganglion neurons. *Biomed. Opt. Express.* 8:4568–4578. https://doi.org/10.1364/BOE.8.004568

Plaksin, M., E. Kimmel, and S. Shoham. 2016. Cell-Type-Selective Effects of Intramembrane Cavitation as a Unifying Theoretical Framework for Ultrasonic Neuromodulation. *eNeuro.* 3. ENEURO.0136-15.2016. https://doi.org/10.1523/ENEURO.0136-15.2016

Prieto, M.L., O. Oralkan, B.T. Khuri-Yakub, and M.C. Maduke. 2013. Dynamic response of model lipid membranes to ultrasonic radiation force. *PLoS One.* 8. e77115. https://doi.org/10.1371/journal.pone.0077115

Prieto, M.L., K. Firouzi, B.T. Khuri-Yakub, and M. Maduke. 2018. Activation of Piezo1 but Not $Na_V1.2$ Channels by Ultrasound at 43 MHz. *Ultrasound Med. Biol.* 44:1217–1232. https://doi.org/10.1016/j.ultrasmedbio.2017.12.020

Qiu, Z., J. Guo, S. Kala, J. Zhu, Q. Xian, W. Qiu, G. Li, T. Zhu, L. Meng, R. Zhang, et al. 2019. The Mechanosensitive Ion Channel Piezo1 Significantly Mediates In Vitro Ultrasonic Stimulation of Neurons. *iScience.* 21:448–457. https://doi.org/10.1016/j.isci.2019.10.037

Rashid, B., M. Destrade, and M.D. Gilchrist. 2012. Mechanical characterization of brain tissue in compression at dynamic strain rates. *J. Mech. Behav. Biomed. Mater.* 10:23–38. https://doi.org/10.1016/j.jmbbm.2012.01.022

Rashid, B., M. Destrade, and M.D. Gilchrist. 2013. Mechanical characterization of brain tissue in simple shear at dynamic strain rates. *J. Mech. Behav. Biomed. Mater.* 28:71–85. https://doi.org/10.1016/j.jmbbm.2013.07.017

Ricca, B.L., G. Venugopalan, and D.A. Fletcher. 2013. To pull or be pulled: parsing the multiple modes of mechanotransduction. *Curr. Opin. Cell Biol.* 25:558–564. https://doi.org/10.1016/j.ceb.2013.06.002

Richter, C.P., A.I. Matic, J.D. Wells, E.D. Jansen, and J.T. Walsh, Jr.. 2011. Neural stimulation with optical radiation. *Laser Photonics Rev.* 5:68–80. https://doi.org/10.1002/lpor.200900044

Sarvazyan, A.P., O.V. Rudenko, and W.L. Nyborg. 2010. Biomedical applications of radiation force of ultrasound: historical roots and physical basis. *Ultrasound Med. Biol.* 36:1379–1394. https://doi.org/10.1016/j.ultrasmedbio.2010.05.015

Schewe, M., E. Nematian-Ardestani, H. Sun, M. Musinszki, S. Cordeiro, G. Bucci, B.L. de Groot, S.J. Tucker, M. Rapedius, and T. Baukrowitz. 2016. A Non-canonical Voltage-Sensing Mechanism Controls Gating in K2P K(+) Channels. *Cell.* 164:937–949. https://doi.org/10.1016/j.cell.2016.02.002

Seeger, H.M., L. Aldrovandi, A. Alessandrini, and P. Facci. 2010. Changes in single K(+) channel behavior induced by a lipid phase transition. *Biophys. J.* 99:3675–3683. https://doi.org/10.1016/j.bpj.2010.10.042

Selfridge, A.R. 1985. Approximate Material Properties in Isotropic Materials. *Ieee T Son Ultrason.* 32:381–394. https://doi.org/SU.1985.31608

Shah, M.M., M. Migliore, I. Valencia, E.C. Cooper, and D.A. Brown. 2008. Functional significance of axonal Kv7 channels in hippocampal pyramidal neurons. *Proc. Natl. Acad. Sci. USA.* 105:7869–7874. https://doi.org/10.1073/pnas.0802805105

Shao, L.R., R. Halvorsrud, L. Borg-Graham, and J.F. Storm. 1999. The role of BK-type Ca2+-dependent K+ channels in spike broadening during repetitive firing in rat hippocampal pyramidal cells. *J. Physiol.* 521:135–146. https://doi.org/10.1111/j.1469-7793.1999.00135.x

Shapiro, M.G., K. Homma, S. Villarreal, C.P. Richter, and F. Bezanilla. 2012. Infrared light excites cells by changing their electrical capacitance. *Nat. Commun.* 3:736. https://doi.org/10.1038/ncomms1742

Tabarean, I.V., and C.E. Morris. 2002. Membrane stretch accelerates activation and slow inactivation in Shaker channels with S3-S4 linker deletions. *Biophys. J.* 82:2982–2994. https://doi.org/10.1016/S0006-3495(02)75639-7

Talley, E.M., G. Solorzano, Q. Lei, D. Kim, and D.A. Bayliss. 2001. Cns distribution of members of the two-pore-domain (KCNK) potassium channel family. *J. Neurosci.* 21:7491–7505. https://doi.org/10.1523/JNEUROSCI.21-19-07491.2001

Taverna, S., T. Tkatch, A.E. Metz, and M. Martina. 2005. Differential expression of TASK channels between horizontal interneurons and pyramidal cells of rat hippocampus. *J. Neurosci.* 25:9162–9170. https://doi.org/10.1523/JNEUROSCI.2454-05.2005

Taylor, R.E. 1965. Impedance of the squid axon membrane. *J. Cell. Comp. Physiol.* 66(S2):21–25. https://doi.org/10.1002/jcp.1030660507

Thijssen, J.M., H.J. Mol, and M.R. Timmer. 1985. Acoustic parameters of ocular tissues. *Ultrasound Med. Biol.* 11:157–161. https://doi.org/10.1016/0301-5629(85)90018-3

Tsui, P.H., S.H. Wang, and C.C. Huang. 2005. In vitro effects of ultrasound with different energies on the conduction properties of neural tissue. *Ultrasonics.* 43:560–565. https://doi.org/10.1016/j.ultras.2004.12.003

Tufail, Y., A. Matyushov, N. Baldwin, M.L. Tauchmann, J. Georges, A. Yoshihiro, S.I. Tillery, and W.J. Tyler. 2010. Transcranial pulsed ultrasound stimulates intact brain circuits. *Neuron.* 66:681–694. https://doi.org/10.1016/j.neuron.2010.05.008

Tyler, W.J., Y. Tufail, M. Finsterwald, M.L. Tauchmann, E.J. Olson, and C. Majestic. 2008. Remote excitation of neuronal circuits using low-intensity, low-frequency ultrasound. *PLoS One.* 3. e3511. https://doi.org/10.1371/journal.pone.0003511

Tyler, W.J., S.W. Lani, and G.M. Hwang. 2018. Ultrasonic modulation of neural circuit activity. *Curr. Opin. Neurobiol.* 50:222–231. https://doi.org/10.1016/j.conb.2018.04.011

Walsh, A.J., G.P. Tolstykh, S. Martens, B.L. Ibey, and H.T. Beier. 2016. Action potential block in neurons by infrared light. *Neurophotonics.* 3. 040501. https://doi.org/10.1117/1.NPh.3.4.040501

Wang, J., and O.P. Hamill. 2020. Piezo2, a pressure sensitive channel is expressed in select neurons of the mouse brain: a putative mechanism for synchronizing neural, networks by transducing intracranial pressure pulses. *bioRxiv.* (Preprint posted March 25, 2020). https://doi.org/10.1101/2020.03.24.006452

Wells, J., C. Kao, P. Konrad, T. Milner, J. Kim, A. Mahadevan-Jansen, and E.D. Jansen. 2007. Biophysical mechanisms of transient optical stimulation of peripheral nerve. *Biophys. J.* 93:2567–2580. https://doi.org/10.1529/biophysj.107.104786

White, S.H., and T.E. Thompson. 1973. Capacitance, area, and thickness variations in thin lipid films. *Biochim. Biophys. Acta.* 323:7–22. https://doi.org/10.1016/0005-2736(73)90428-8

Wu, J., and W.L. Nyborg. 2008. Ultrasound, cavitation bubbles and their interaction with cells. *Adv. Drug Deliv. Rev.* 60:1103–1116. https://doi.org/10.1016/j.addr.2008.03.009

Yamada-Hanff, J., and B.P. Bean. 2015. Activation of Ih and TTX-sensitive sodium current at subthreshold voltages during CA1 pyramidal neuron firing. *J. Neurophysiol.* 114:2376–2389. https://doi.org/10.1152/jn.00489.2015

Ye, P.P., J.R. Brown, and K.B. Pauly. 2016. Frequency Dependence of Ultrasound Neurostimulation in the Mouse Brain. *Ultrasound Med. Biol.* 42:1512–1530. https://doi.org/10.1016/j.ultrasmedbio.2016.02.012

Yoo, S., D.R. Mittelstein, R. Hurt, J. Lacroix, and M.G. Shapiro. 2020. Focused ultrasound excites neurons via mechanosensitive calcium accumulation and ion channel amplification. *bioRxiv.* (Preprint posted May 22, 2020). https://doi.org/10.1101/2020.05.19.101196

Young, R.R., and E. Henneman. 1961. Functional effects of focused ultrasound on mammalian nerves. *Science.* 134:1521–1522. https://doi.org/10.1126/science.134.3489.1521

Yue, C., and Y. Yaari. 2004. KCNQ/M channels control spike after-depolarization and burst generation in hippocampal neurons. *J. Neurosci.* 24:4614–4624. https://doi.org/10.1523/JNEUROSCI.0765-04.2004

Zachs, D.P., S.J. Offutt, R.S. Graham, Y. Kim, J. Mueller, J.L. Auger, N.J. Schuldt, C.R.W. Kaiser, A.P. Heiller, R. Dutta, et al. 2019. Noninvasive ultrasound stimulation of the spleen to treat inflammatory arthritis. *Nat. Commun.* 10:951. https://doi.org/10.1038/s41467-019-08721-0

Zhou, D., S. Lambert, P.L. Malen, S. Carpenter, L.M. Boland, and V. Bennett. 1998. AnkyrinG is required for clustering of voltage-gated Na channels at axon initial segments and for normal action potential firing. *J. Cell Biol.* 143:1295–1304. https://doi.org/10.1083/jcb.143.5.1295

Zhu, X., J.W. Lin, and M.Y. Sander. 2019. Infrared inhibition and waveform modulation of action potentials in the crayfish motor axon. *Biomed. Opt. Express.* 10:6580–6594. https://doi.org/10.1364/BOE.10.006580

Supplemental material

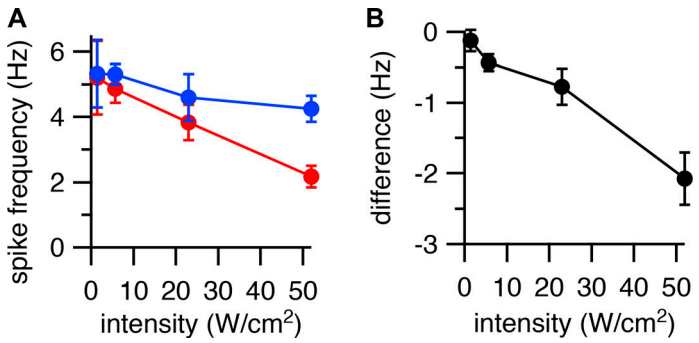

Figure S1. **Effects of ultrasound at different intensities on firing rate. (A)** Mean (± SEM) action potential firing rate with (red) or without (blue) a 1-s ultrasound pulse at various intensities starting 200 ms after the start of a 2-s current step, as measured during the period of overlap between the ultrasound and current stimuli, or during the same time period in the absence of ultrasound. *n* = 4 cells, except for 6 W/cm^2, where *n* = 3 cells. **(B)** As in A, but showing the difference in firing rate between the ultrasound and control conditions.

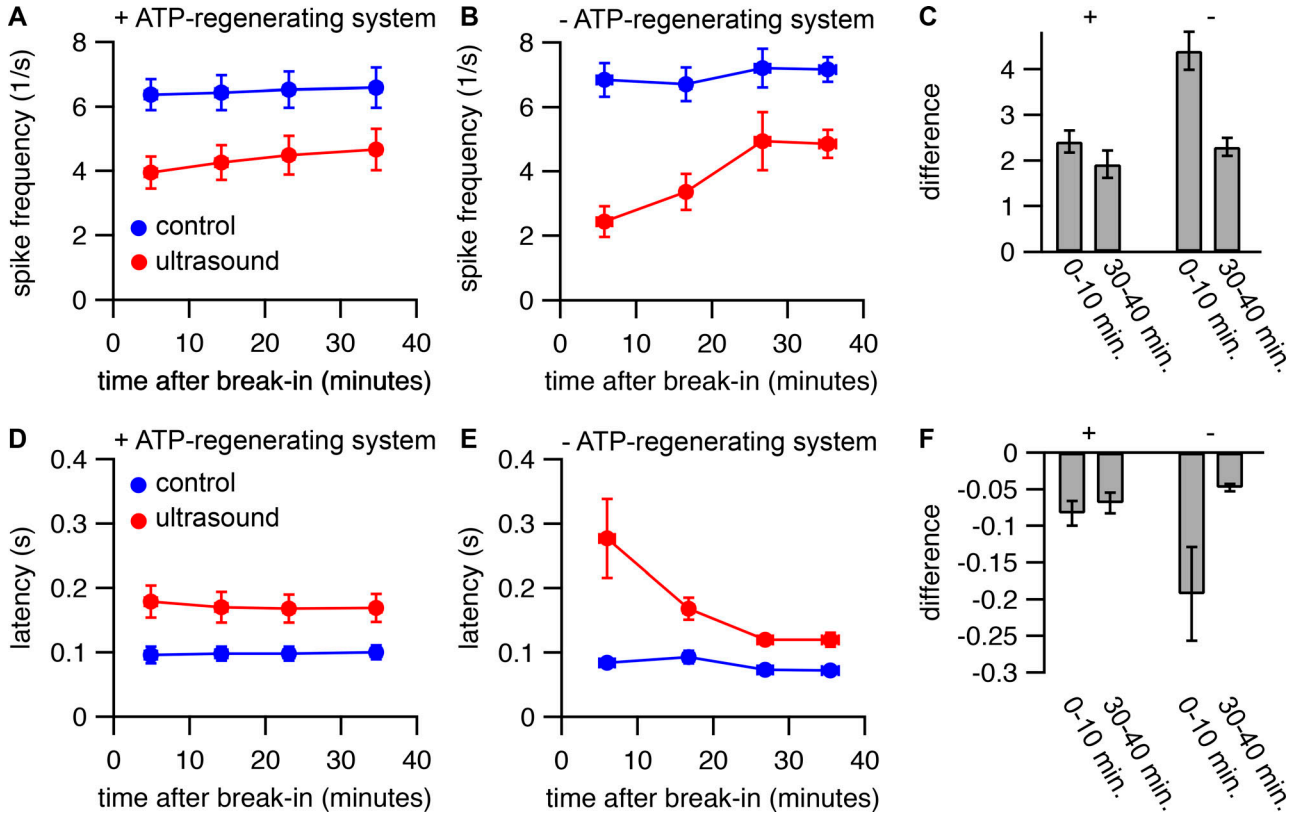

Figure S2. **An ATP-regenerating internal solution stabilizes the response to ultrasound. (A and B)** Mean (± SEM) spike rates during the first 500 ms of a current step in the presence (red circles) and absence (blue circles) of a 1-s ultrasound application starting 500 ms before the current step, as a function of time relative to break-in (establishment of whole-cell recording configuration). The internal solution contained 10 Na-phosphocreatine with (A) or without (B) 50 U/ml creatine phosphokinase to provide an ATP-regenerating system. Spike rates were measured at various time points between 0 and 10, 10 and 20, 20 and 30, and 30 and 40 min after break-in. The x values represent the mean start time for the protocol to measure spike rates (which comprised 2 min of recording time) with horizontal error bars (in some cases smaller than the symbol size) representing the SEM. The amplitude of the current step was adjusted over time to maintain spiking behavior as close as possible to that at the start of the experiment. **(C)** Mean (± SEM) difference in spike rate between the control and ultrasound conditions for measurements at 1–10 min after break-in and 30–40 min after break-in, with (left) or without (right) the ATP-regenerating system. The difference was only statistically significant without the ATP-regenerating system (P = 0.11, with; and P = 0.0064, without). **(D–F)** Same as A–C, but for latency to the first action potential following the start of the current step. *n* = 10 cells with and *n* = 6 cells without the ATP-regenerating system. The difference was not statistically significant for either group (P = 0.21, with; and P = 0.089, without).

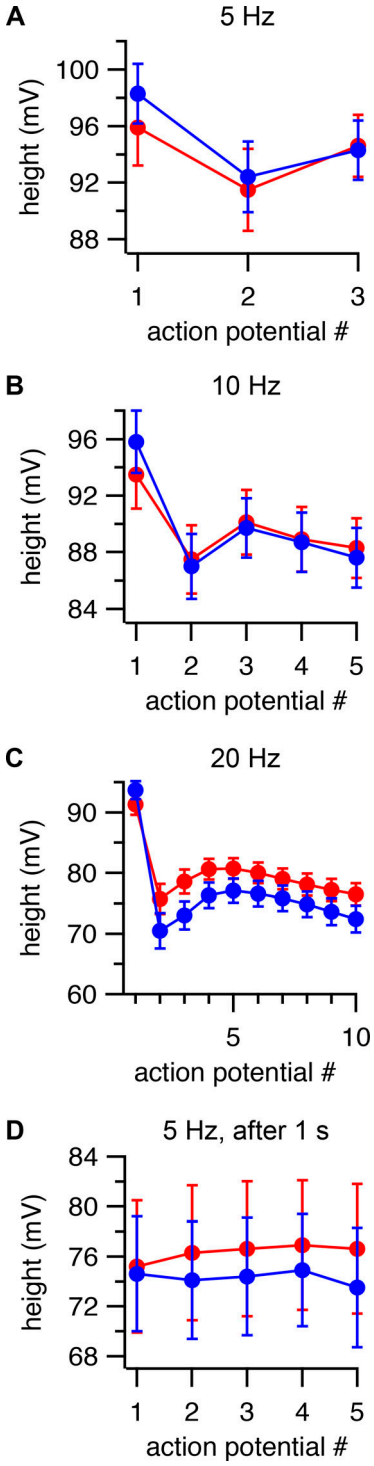

Figure S3. **Effects of ultrasound on action potential height. (A–C)** Mean (± SEM) action potential heights as a function of action potential number in the presence (red) and absence (blue) of a 1-s ultrasound pulse starting 500 ms before the current step, for cells firing at an average firing rate (as measured during the first 500 ms of the current step) of ∼5 Hz (n = 13), 10 Hz (n = 15), and 20 Hz (n = 13) in the control condition. **(D)** As in A–C, but with ultrasound applied 1 s after the start of a 3-s current step, for cells firing at an average firing rate of ∼5 Hz in the control condition, with firing rate determined in a 1-s window starting 1 s after the current step (corresponding to the time period of the ultrasound stimulus), and action potential number relative to the start of the ultrasound stimulus (n = 6). Note that the y axes do not begin at zero.

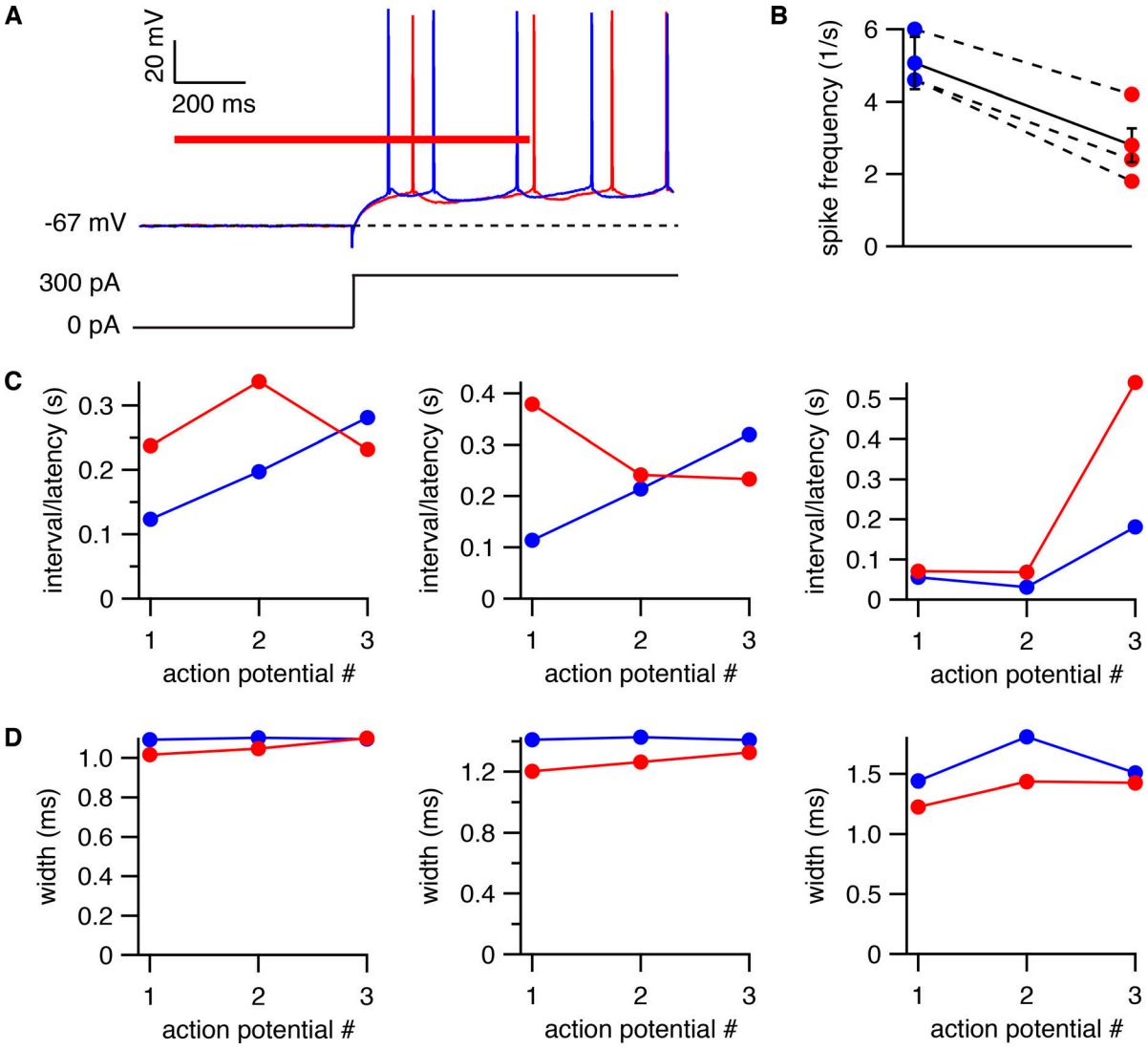

Figure S4. **Effects of ultrasound on action potential firing and waveform at near-physiological temperature. (A)** Example voltage traces showing inhibition of action potential firing by ultrasound at 30°C. The response to a 300-pA current step is shown with (red voltage trace) and without (blue voltage trace) a 1-s ultrasound pulse (red bar) applied 500 ms before the start of the current step. The dashed line indicates the resting membrane voltage. **(B)** Mean (± SEM, n = 3) spike frequency during the first 500 ms of the current step (corresponding to the period of overlap between the current and ultrasound stimuli, or the equivalent time period in the absence of ultrasound) for the protocol shown in A for the control (blue) and ultrasound (red) conditions, for cells firing at an average spike frequency of ∼5 Hz in the absence of ultrasound. Data points for the individual cells are shown connected by dashed lines (compare to Fig. 1 E). **(C)** Latency between the start of the current step and the first action potential, and between the first and second, and second and third action potentials, for the control (blue) and ultrasound (red) conditions for three individual cells (compare to Fig. 4 A). **(D)** As in C, but for effects of ultrasound on action potential width (compare to Fig. 6 A).